

ABSTRACT

Title of dissertation: Measuring topology of BECs
in a synthetic dimensions lattice

Dina Genkina
Doctor of Philosophy, 2018

Dissertation directed by: Professor Ian Spielman
Department of Physics

Measuring topology of BECs in a synthetic dimensions lattice

by

Dina Genkina

Dissertation submitted to the Faculty of the Graduate School of the
University of Maryland, College Park in partial fulfillment
of the requirements for the degree of
Doctor of Philosophy
2018

Advisory Committee:
Professor Ian Spielman, Chair/Advisor

© Copyright by
Dina Genkina
2018

Table of Contents

List of Tables	8
List of Figures	9
1 Introduction	1
1.1 Condensed matter context	1
1.1.1 Topology	2
1.1.2 Band topology in materials	3
1.1.3 Quantum Hall Effect	5
1.1.4 Hofstadter regime	6
1.2 Ultracold atoms for quantum simulation	6
2 Atom Light Interactions	7
2.1 Atomic structure	7
2.1.1 Fine and hyperfine structure	7
2.1.2 Interaction with static magnetic fields	8
2.2 Near-resonant atom-light interaction	13
2.2.1 Rabi oscillations	13
2.2.2 Scattering	16
2.2.3 Adiabatic rapid passage	16
2.3 Far-off resonant atom-light interaction	18
2.4 Absorption imaging	19
2.4.1 Time-of-flight and in situ imaging	22
2.5 One dimensional optical lattices	23
2.5.1 Lattice Hamiltonian	23
2.5.2 Tight binding approximation	27
2.5.3 Pulsing vs adiabatic loading of the lattice	28
2.6 Raman and rf coupling	33
2.6.1 Rf coupling Hamiltonian	33
2.6.2 Raman coupling Hamiltonian	35
2.6.3 Calibration of Raman and Rf dressed states	38

3	Ultracold Gases and the RbK apparatus	44
3.1	Bose-Einstein condensation	44
3.1.1	Phase transition of a non-interacting Bose gas	44
3.1.2	Interacting Bose gas	49
3.2	Degenerate Fermi Gas	53
3.2.1	Fermi statistics and the onset of degeneracy	53
3.2.2	Interactions and Feshbach resonances	55
3.3	RbK apparatus	58
3.3.1	Laser beams	60
3.3.2	Magnetic coils	62
3.3.3	Procedure for making a BEC	64
3.3.4	Changes to apparatus for Rubidium	66
3.3.4.1	Master laser setup	67
3.3.4.2	Alignment imaging path	69
3.3.4.3	FPGA quad servo	73
3.3.4.4	ODT beam shaping	75
3.3.5	Procedure for making a DFG	78
3.3.6	Current status of Potassium apparatus	81
4	Absorption Imaging with Recoil Induced Detuning	88
4.1	Recoil-induced detuning	88
4.2	Perturbative treatment	89
4.3	Stationary atom model	90
4.4	Traveling atom model	95
4.5	Calibration of saturation intensity	96
4.6	SNR optimization	99
5	Direct Imaging of Scattering Near a Feshbach Resonance	102
5.1	Experimental procedure	103
5.2	Data analysis	106
5.3	Results	109
6	Synthetic Magnetic Fields in Synthetic Dimensions	111
6.1	Synthetic dimensions setup	112
6.2	Hamiltonian of the effective 2-D system	115
6.2.1	Hamiltonian	115
6.2.2	Band structure	118
6.2.3	Calibration	121
6.2.4	Tight binding approximation	124
6.3	Eigenstates of the synthetic 2-D lattice	126
6.4	Chiral edge currents	128
6.5	Observation of skipping orbits	131

7	Measuring Chern Number in Synthetic Dimensions	134
7.1	Experimental procedure	135
7.1.1	Loading procedures	137
7.1.2	Application of force and measurement	139
7.1.3	Density reduction	142
7.1.4	Rf correction	143
7.2	Quantum Hall Effect interpretation	145
7.2.1	Microscoping view of QHE	145
7.2.2	Chern number from Hall conductivity	147
7.2.3	Inadequacy for narrow systems	147
7.3	Measuring Chern number via Diophantine equation	150
7.3.1	TKNN Diophantine equation in synthetic dimensions	151
7.3.2	Prescription for identifying Chern number	152
7.3.3	Properties of the method	154
7.4	Results and conclusion	155
	Bibliography	158

List of Tables

List of Figures

1	Topology of baked goods	3
2	5
1	Atomic structure of the ground and first excites states	9
2	Energy structure of hyperfine states of ^{87}Rb	11
3	Adiabatic rapid passage (ARP)	17
4	Absorption imaging	20
5	Lattice band structure in the extended zone scheme	26
6	Lattice pulsing	30
7	Lattice pulsing for calibration	31
8	Adiabatic lattice loading	32
9	Raman and rf coupling schematic	34
10	Band structure of the rf Hamiltonian	36
11	Band structure of the Raman Hamiltonian	39
12	Pulsing on rf coupling	41
13	Pulsing on Raman coupling	42
1	Occupation of energy states of a 3-D harmonic oscillator	47
2	Time-of-flight images of atoms	48
3	In situ measurement of a fraction of bose condensed atoms	52
4	Occupation number as a function of energy for a Fermi gas	55
5	Schematic of a Feshbach resonance	57
6	Photograph of RbK apparatus at NIST Gaithersburg	59
7	Schematic of RbK apparatus	61
8	Schematic of magnetic coils on the RbK apparatus	63
9	New master board layout	67
10	Schematic of the bottom half of the alignment imaging system	70
11	Schematic of the new imaging lens	71
12	Schematic of the top half of the alignment imaging system	72
13	Turn on and off curves of the quad coils	76
14	Output current as a function of computer command voltage	77
15	Schematic of beam shaping optics in the path of the 0th order ODT beam	77

16	Beam waist as a function of propagation distance	79
17	Schematic of the 2D MOT setup	83
18	Picture of 2D MOT cell	84
19	Schematic of 2D MOT optics	86
20	Picture of current 2D MOT apparatus	87
1	Recoil induced detuning	91
2	Optical depth as a function of probe intensity	93
3	Checking stationary atom assumption	94
4	Phase space evolution of the atomic cloud	97
5	Comparison of stationary and moving atom simulations	98
6	Signal-to-noise optimization	101
1	An sample absorption image after 6.8 ms TOF	106
2	Experimental setup and inverse Abel transform	107
3	Normalized scattered population vs bias field B	110
1	Setup of effective 2-D lattice	113
2	Band structure of the synthetic dimensions Hamiltonian	119
3	Calibration of synthetic dimesnions lattice	122
4	Band structure of the tight binding versus full Hamiltonian	125
5	Eigenstates of the synthetic dimensions lattice	127
6	Measuring chiral currents in synthetic dimensions	130
7	Imaging skipping orbits	132
1	Quantum Hall effect in Hofstadter ribbons	136
2	Band structure of the lattice-coupled system in $F = 2$	138
3	Application of a constant force by displacing a Gaussian beam potential	140
4	Band structure in a 5-site wide ribbon	141
5	Correction of oscillations in rf coupled data	144
6	Hall displacement	148
7	Band structure of the synthetic dimesnions lattice with flux $\Phi/\Phi_0 = -4/3$	149
8	Chern number from the TKNN equation	151
9	Calculating Chern number	153
10	Chern number dependence	155
11	Chern number measurement	156

Chapter 3: Ultracold Gases and the RbK apparatus

In this chapter we introduce the basics of ultracold quantum gases. When cooled to extremely low temperatures, bosonic atoms form Bose Einstein condensates, described in sec. ???. Fermionic atoms do not undergo a phase transition, but gradually become degenerate, forming what's known as a degenerate Fermi Gas, described in sec. ???. We then give a basic overview of the rubidium-potassium (RbK) apparatus at NIST, on which the work described in this thesis was done, in sec. ???. We detail some of the changes that have been made to the apparatus since it was last documented.

3.1 Bose-Einstein condensation

In this section, we give some basic background on Bose-Einstein condensation, relevant to ^{87}Rb atoms cooled in our apparatus.

3.1.1 Phase transition of a non-interacting Bose gas

Bose gases are characterized by the Bose-Einstein distribution giving the number of atoms $n(E_j)$ occupying each energy eigenstate E_j as

$$n(E_j) = \frac{1}{e^{(E_j - \mu)/k_B T} - 1}, \quad (3.1)$$

where k_B is the Boltzmann constant, T is the temperature in Kelvin, and μ is the chemical potential. Assuming the total atom number N is fixed, the chemical

potential $\mu(T, N)$ ensures that the total occupation $\sum_j n(E_j) = N$.

The Bose distribution leads to Bose-Einstein condensation, the collapse of a macroscopic fraction of the atoms into the ground state. This comes as a direct consequence of the Bose distribution's characteristic -1 in the denominator. Consider the occupation number $n(E_j)$. It must remain positive, as a negative occupation number is unphysical. This implies the quantity $e^{(E_j - \mu)/k_B T}$ must remain greater than 1, or $(E_j - \mu)/k_B T > 0$ for all E_j . Therefore, $\mu \leq E_0$, where E_0 is the ground state energy.

Then, for a given temperature T , there is a maximum occupation number for each excited state given by $n(E_j) = \frac{1}{e^{E_j/k_B T} - 1}$. The only energy state whose occupation number is unbounded is the ground state, as $n(E_0)$ tends toward infinity as μ tends towards 0. Therefore, as the temperature decreases, the maximum occupation of each excited state decreases until they can no longer support all N of the atoms. The remaining atoms then have no choice but to collapse into the lowest energy level and Bose condense.

We will show this quantitatively for the case of a 3-D harmonically trapped gas of atoms, relevant to the experiments described in this thesis. It is convenient to define the fugacity $\zeta = e^{\mu/k_B T}$, and re-write the Bose-Einstein distribution for some eigenstate E_j as

$$n(E_j) = \frac{\zeta}{e^{E_j/k_B T} - \zeta}. \quad (3.2)$$

The harmonic oscillator potential can be written as

$$V(r) = \frac{1}{2}m(\omega_x^2x^2 + \omega_y^2y^2 + \omega_z^2z^2), \quad (3.3)$$

where ω_x , ω_y and ω_z are the angular trapping frequencies along \mathbf{e}_x , \mathbf{e}_y , and \mathbf{e}_z . The

eigenenergies with this potential are

$$E(j_x, j_y, j_z) = \left(\frac{1}{2} + j_x\right)\hbar\omega_x + \left(\frac{1}{2} + j_y\right)\hbar\omega_y + \left(\frac{1}{2} + j_z\right)\hbar\omega_z. \quad (3.4)$$

In order to find μ , we must find $\sum_{j_x, j_y, j_z} n(E(j_x, j_y, j_z))$ and set it equal to N . This task is greatly simplified by going to the continuum limit and finding the density of states. To do this, we neglect the zero-point energy (setting $E_0 = 0$, the effects of the zero-point energy are discussed in [13] section 2.5) and assume there is on average one state per volume element $\hbar^3\omega_x\omega_y\omega_z$. Then, the total number of states with energy less than or equal to some value ϵ is given by the volume of a prism made between points $(x, y, z) = (0, 0, 0), (\epsilon, 0, 0), (0, \epsilon, 0)$ and $(0, 0, \epsilon)$ in units of the volume element:

$$G(\epsilon) = \frac{\epsilon^3}{6\hbar^3\omega_x\omega_y\omega_z}. \quad (3.5)$$

The density of states is given by

$$g(\epsilon) = \frac{d}{d\epsilon}G(\epsilon) = \frac{\epsilon^2}{3\hbar^3\omega_x\omega_y\omega_z}. \quad (3.6)$$

Note that the occupation of the ground state is not included in this continuum picture. We can therefore use it only to calculate the total number of atoms in all of the excited states:

$$N_{\text{ex}} = \int_0^\infty d\epsilon g(\epsilon)n(\epsilon) = \int_0^\infty d\epsilon \frac{\epsilon^2}{3\hbar\omega_x\omega_y\omega_z} \frac{\zeta}{e^{\epsilon/k_B T} - \zeta} = \frac{(k_B T)^3}{\hbar^3\omega_x\omega_y\omega_z} \text{Li}_3(\zeta), \quad (3.7)$$

where $\text{Li}_3(\zeta)$ is the polylogarithm function¹. We define the mean trapping frequency $\bar{\omega} = (\omega_x\omega_y\omega_z)^{1/3}$ and the harmonic oscillator energy as $\hbar\bar{\omega}$, with the thermal energy

¹This calculation was done with Wolfram Alpha, not Russian algebra skills

in harmonic oscillator units $\tau = k_B T / \hbar \bar{\omega}$, giving

$$N_{\text{ex}} = \tau^3 \text{Li}_3(\zeta). \quad (3.8)$$

Finding the occupation number of the ground state from the Bose-Einstein distribution

$$N_0 = \frac{\zeta}{1 - \zeta}, \quad (3.9)$$

we can then find the chemical potential, or equivalently the fugacity ζ , to satisfy

$$N = N_0 + N_{\text{ex}}. \quad (3.10)$$

This is a transcendental equation that can only be solved numerically. We present an example of the solution in Figure 1. Here, we have calculated the fractional population in different harmonic oscillator energy levels for three different temperatures, using trapping frequencies $\omega_x = \omega_y = \omega_z = 2\pi \times 50$ Hz, and atom number $N = 10^6$. For energies above the ground state (dots in the figure), we binned 50 energy levels together, such that each dot represents the total fractional population in 50 adjacent levels. This was obtained by integrating eqn. 3.7 from $\epsilon - 25\hbar\bar{\omega}$ to $\epsilon + 25\hbar\bar{\omega}$. The stars represent the fractional population in just the ground state, calculated from eqn. 3.9. Note that at temperature $T = 255$ nK (red), the ground state population is consistent with a continuous extrapolation from the excited state populations and is almost zero. At lower temperatures, $T = 180$ nK (blue) the ground state population is in excess of any reasonable extrapolation from the excited state fractions, and at $T = 80$ nK (green) almost all the atoms are in the ground state.

The onset of Bose-Einstein condensation occurs at a critical temperature T_c . This temperature is defined as the temperature at which the occupation number of excited states is equal to the atom number, i.e. when the atoms have occupied all

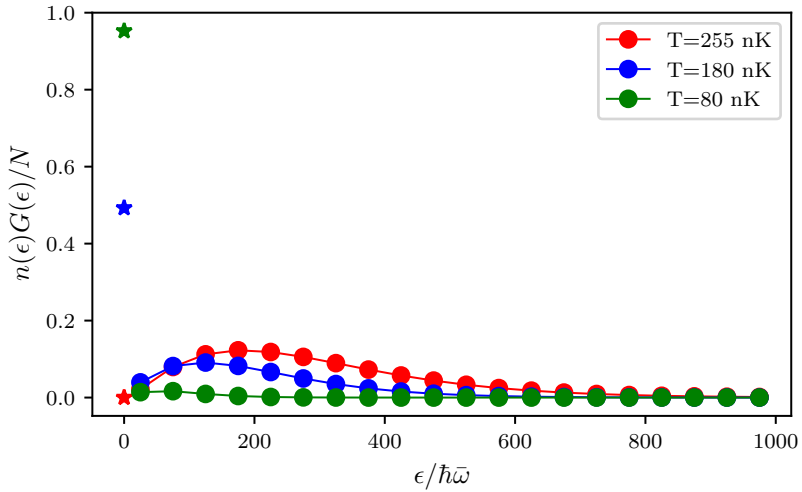


Figure 1: Occupation of energy states of a 3-D harmonic oscillator. The trapping frequencies are $\omega_x = \omega_y = \omega_z = 2\pi \times 50$ Hz, and the atom number is $N = 10^6$. Dots represent the total fractional population in 50 adjacent energy levels, including degeneracies. The stars represent the fractional population in just the ground state.

available excited states and any remaining atoms were forced to pile into the ground state. Since the maximal occupation of the excited states will occur at $\mu = 0$, the occupation of the excited state is bounded from above by $N_{\text{ex}}(\mu = 0)$, and the critical temperature is defined by

$$N = N_{\text{ex}}(\mu = 0, T = T_c) = \frac{(k_B T_c)^3}{\hbar^3 \omega_x \omega_y \omega_z} \text{Li}_3(\zeta = 1). \quad (3.11)$$

Using $\text{Li}_3(1) \approx 1.202$, we obtain for a given atom number and trapping frequencies

$$T_c = \frac{1.202 N}{k_B^3} \hbar^3 \omega_x \omega_y \omega_z. \quad (3.12)$$

For the parameters in Figure 1, $T_c = 225$ nK.

For temperatures below the critical temperature, the condensation fraction f_c —the fraction of atoms in the ground state—is directly related to the ratio of the

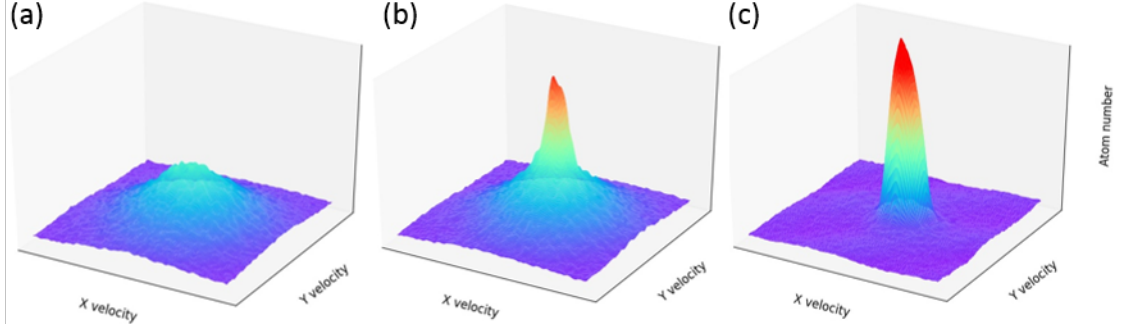


Figure 2: Time-of-flight images of atoms. (a) Above the critical temperature - the atoms are thermally distributed. (b) Below the critical temperature - about half of the atoms are condensed in the central peak. (c) Far below the critical temperature - almost all atoms are condensed in the central peak.

temperature to the critical temperature:

$$f_c = 1 - \frac{N}{N_{\text{ex}}} = 1 - \frac{(k_B T)^3}{\hbar^3 \omega_x \omega_y \omega_z} \text{Li}_3(\zeta = 1) = 1 - \left(\frac{T}{T_c} \right)^3, \quad (3.13)$$

where in the last step we have plugged in the definition of the critical temperature eqn. 3.12.

Figure 2 shows the progression towards condensation as the temperature of a cloud of ^{87}Rb is decreased below T_c . The images are obtained via a time-of-flight measurement (see section 2.4.1), where the atoms are allowed to expand freely, mapping the initial momentum to final position, imaged via absorption imaging (see section 2.4). The x and y axes represent momentum along x and y , while the z axis represents the number of atoms. The z axis momentum is integrated over. Figure 2a shows a cloud above the condensation temperature - the momentum distribution is gaussian, given by the Maxwell-Boltzmann distribution. In fig. 2b, the temperature has been decreased below T_c , and about half the atoms have collapsed into the ground state, producing a large peak in atom number around zero momentum. In fig. 2c, the temperature has been decreased even further and almost all the atoms populate the central peak - the distribution is no longer gaussian but a sharp peak

around zero momentum.

3.1.2 Interacting Bose gas

In the previous section, we assumed there were no interaction between the atoms other than those enforced by statistics. In this section, we will relax this assumption somewhat and describe the condensed atomic state through its characteristic Gross-Pitaevskii equation.

Since condensation occurs at very low temperatures, and thus very low kinetic energies, we can assume that any scattering processes between the atoms are *s*-wave and can be described simply by a scattering length a . For ^{87}Rb , relevant to experiments described in this thesis, the scattering length between two atoms in the $F = 2$ hyperfine state is $a = 95.44(7)a_0$ [14], where $a_0 = 5.29 \times 10^{-11}$ m is the Bohr radius. The short-range interaction between two particles can be approximated as a contact interaction with an effective strength U_0 as (see [13] section 5.2.1):

$$U(r_1, r_2) = U_0\delta(r_1 - r_2) = \frac{4\pi\hbar^2 a}{m}\delta(r_1 - r_2), \quad (3.14)$$

where m is the atomic mass and δ is the Dirac delta function. The full Hamiltonian of the many-body system is then

$$H = \sum_i \frac{p_i^2}{2m} + V(r_i) + U_0 \sum_{i < j} \delta(r_i - r_j), \quad (3.15)$$

where i labels the particles, p_i is the momentum, r_i is the position, and V is the external potential.

We make the mean field approximation by assuming that no interactions between two atoms take them out of the ground state, and hence all atoms can be assumed to be in the same single particle wavefunction, making the overall wave-

function

$$\Psi(r_1, r_2, \dots, r_N) = \prod_i^N \phi(r_i), \quad (3.16)$$

where ϕ is the single particle wavefunction. It is convenient to define the wavefunction of the condensed state, $\psi(r) = \sqrt{N}\phi(r)$, making the normalization $N = \int dr |\psi(r)|^2$.

The energy of this wavefunction under the Hamiltonian above is given by

$$E = \int dr \left[\frac{\hbar^2}{2m} |\nabla \psi(r)|^2 + V(r) |\psi(r)|^2 + \frac{1}{2} U_0 |\psi(r)|^4 \right]. \quad (3.17)$$

Given N particles, there are $N(N - 1)/2$ unique pairs of particles that can have a pairwise interactions, approximately equal to $N^2/2$ for large N . The N^2 is absorbed into the definition of ψ , but the factor of $1/2$ remains on the final interaction term. The task of finding the condensate eigenstate reduces to minimizing this energy under the normalization constraint $N = \int dr |\psi(r)|^2$. This can be done by using the method of Lagrange multipliers to minimize $E - \mu N$. Then, we can minimize this quantity by finding the point where the derivative with respect to ψ and ψ^* is zero. Taking the derivative with respect to ψ^* we obtain

$$-\frac{\hbar^2}{2m} \nabla^2 \psi(r) + V(r) \psi(r) + U_0 |\psi(r)|^2 \psi(r) = \mu \psi(r), \quad (3.18)$$

which is the Gross-Pitaevskii equation. This is a non-linear equation that generally needs to be solved numerically.

There is another approximation that can be made in cases where the atomic density is high enough that the interaction energy is significantly larger than the kinetic energy. Then, the kinetic term in the Hamiltonian can be neglected. This is called the Thomas-Fermi approximation. In this approximation, the wavefunction

is given simply by

$$|\psi(r)|^2 = \frac{\mu - V(r)}{U_0}. \quad (3.19)$$

Here, the probability density simply takes the shape of the interted potential in which the atoms are held. In the case of a harmonically trapped BEC, it is shaped like an inverted parabola. The Thomas-Fermi radius, i.e. the extent of the particle wavefuntion, is the point where the probability density goes to zero: $\mu - V(r_0) = 0$. For a harmonic trap, along any direction, this is given by $r_0^2 = 2\mu/m\omega^2$.

Figure 3a shows an absorption image of a small fraction of a BEC in situ (see section 2.4.1), meaning as it is in the trap - without expanding in time-of-flight. The x and y axes represent position, while color represents the atom number. Figure 3b shows the atom number integrated over the y-axis in blue. The red dashed lines represent the best fit line to a Thomas-Fermi distribution, here an inverted parabola. The black dashed lines represent the best fit of a Gaussian to the atomic distribution. The Thomas-Fermi distirbution matches the atomic distribution more closely in the center where the density is high, but the Gaussian distribution does a better job at the tails of the distribution. This is due to the presence of some fraction of uncondensed atoms, which remain Maxwell-Boltzmann distributed.

3.2 Degenerate Fermi Gas

In this section, we give some basic background on degenerate Fermi gases, relevant to ^{40}K atoms cooled in our apparatus.

3.2.1 Fermi statisctcs and the onset of degeneracy

The occupation of different energy levels E_j by Fermions is given by the Fermi-Dirac distribution:

$$n(E_j) = \frac{1}{e^{(E_j-\mu)/k_B T} + 1}. \quad (3.20)$$

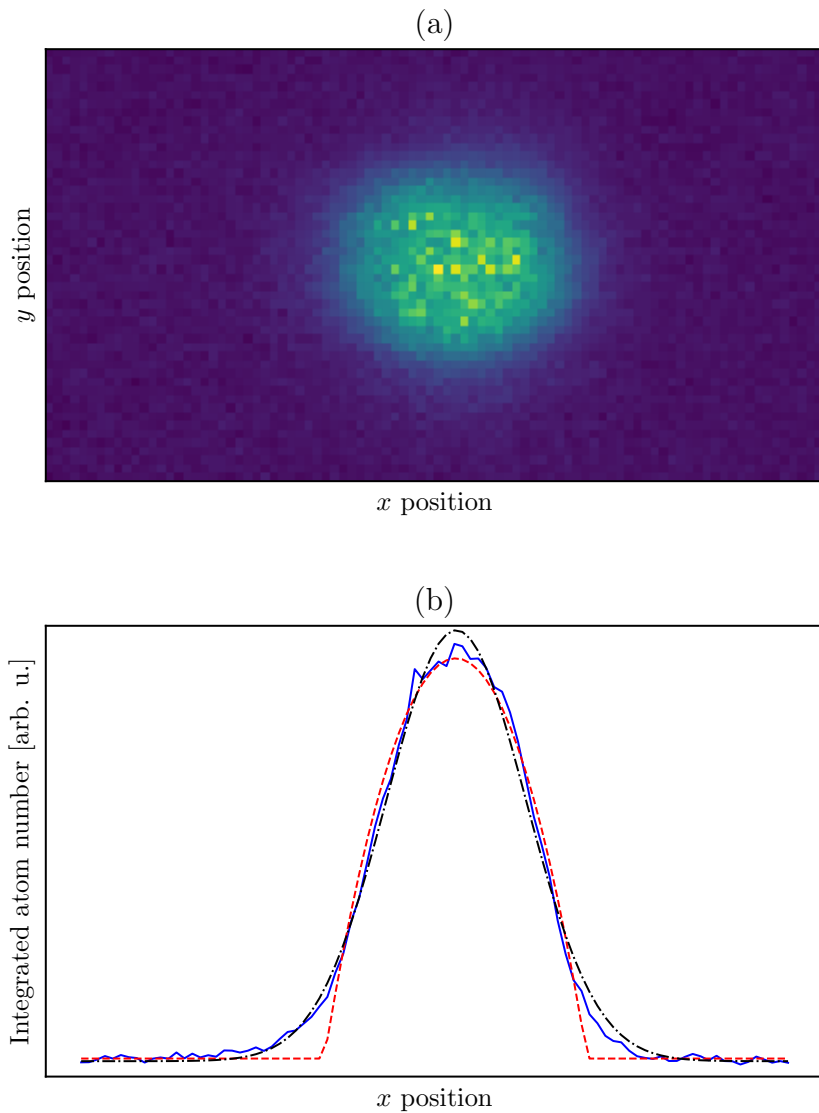


Figure 3: In situ measurement of bose condensed atoms. (a) Absorption image taken of $\approx 1\%$ of the cloud. The x and y axes represent x and y position, while color represents the atom number. (b) The blue line represents atom number as a function of position along the x axis, integrated over the y axis. The black dashed line represents the best fit of a Gaussian function to the atomic distribution. The dashed red line represents the best fit of a Thomas-Fermi profile to the atomic distribution.

The difference from the Bose-Einstein distribution is simply the sign of the 1 in the denominator. This has important implications, however. First, since e^x varies between 0 and ∞ , the occupation $n(E_j)$ varies between 1 and 0 - a consequence of the Pauli exclusion principle. Second, as the temperature T tends towards 0, there become two distinct cases: $E_j - \mu > 0$ and $E_j - \mu < 0$. If $E_j - \mu > 0$, $e^{(E_j-\mu)/k_B T}$ tends towards ∞ , and $n(E_j)$ tends towards 0. If $E_j - \mu < 0$, $e^{(E_j-\mu)/k_B T}$ tends towards 0, and $n(E_j)$ tends towards 1. Therefore, at $T = 0$, the energy states below the chemical potential μ are maximally occupied (with probability 1) and the energy states above the chemical potential are unoccupied.

We can use this to determine the chemical potential at $T = 0$ by constraining the total atom number:

$$N = \sum_j n(E_j) = \sum_{E_j < \mu} 1. \quad (3.21)$$

Again, we take the common example of the 3-D harmonic trap. Then the task reduces to simply finding the number of energy levels at or below a certain energy μ . This is given by eqn. 3.5. From this, we find the chemical potential at zero energy, which is known as the Fermi energy E_F , as

$$E_F = (6N)^{1/3} \hbar \bar{\omega}, \quad (3.22)$$

where $\bar{\omega} = (\omega_x \omega_y \omega_z)^{1/3}$ is the geometric mean of the three trapping frequencies. From the Fermi energy, we can define the associated Fermi temperature T_F as

$$T_F = \frac{(6N)^{1/3} \hbar \bar{\omega}}{k_B}, \quad (3.23)$$

and the Fermi momentum $\hbar k_F$ as

$$\hbar k_F = \sqrt{2m E_F}, \quad (3.24)$$

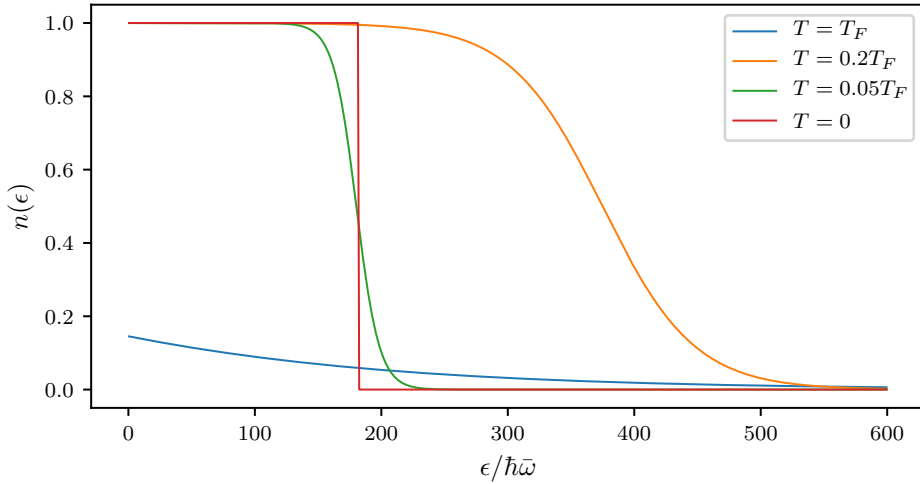


Figure 4: Occupation number as a function of energy for a Fermi gas of $N = 10^6$ atoms in a 3-D harmonic oscillator with frequencies $\omega_x = \omega_y = \omega_z = 2\pi \times 50$ Hz. The Fermi temperature for these parameters is $T_F = 436$ nK.

where m is the mass of the Fermion.

For higher temperatures, we can solve for the chemical potential, or the fugacity ζ , by integrating the Fermi-Dirac distribution weighted by the density of states (eqn. 3.6) to obtain

$$N = \int_0^\infty \frac{\epsilon^2}{2\hbar^3\bar{\omega}^3} \frac{\zeta}{e^{\epsilon/k_B T} + \zeta} = -\frac{(k_B T)^3}{\hbar^3\bar{\omega}^3} \text{Li}_3(-\zeta), \quad (3.25)$$

where Li_3 is again the polylogarithm function. Again, this is a transcendental equation that can be solved numerically. However, in contrast to the BEC case, we do not have to consider the ground state occupation separately, as it is bounded by 1 like every other state.

We show an example of the occupation distribution for different temperatures in Figure 4. Here, we have used the same parameter values as for the BEC case: $N = 10^6$ and $\omega_x = \omega_y = \omega_z = 2\pi \times 50$ Hz. The Fermi temperature for these parameters is $T_F = 436$ nK. For illustrative purposes, we plot $n(\epsilon)$, unweighted by

the density of states $g(\epsilon)$. At zero temperature (red line in the figure), only states below the Fermi energy are occupied. At higher temperatures, the distribution is smoothed out (green and orange lines) until at the Fermi temperature there is almost no significance to the Fermi energy.

In contrast with Bose-Einstein condensation, the transition to a Degenerate Fermi Gas (DFG) is not a phase transition, and there is no absolute measure of the onset of degeneracy. Instead, a Fermi gas can be considered degenerate when the occupation function $n(\epsilon)$ differs significantly from that of a thermal gas. This occurs when the temperature is of order $0.2T_F$.

3.2.2 Interactions and Feshbach resonances

Although the magnitude of the contact interaction U_0 for DFGs is not intrinsically different from that of BECs, there are two key differences. First, the Pauli exclusion principle forbids s -wave interactions between atoms of the same spin. Higher partial wave interactions are 'frozen out' at low temperatures, when the impact parameter of the collision becomes larger than the effective cross section of interactions (see [15], sec. 2.1.2). Therefore, in order to observe interactions, and indeed to cool the gas to degeneracy, another species needs to be present so that intraspecies s -wave interactions can occur. This can be a different atomic species or a different spin state of the same atom.

Second, the densities of standard DFGs ($\approx 10^{12}$ atoms/cm 3) are much lower than that of BECs ($\approx 10^{14}$ atoms/cm 3). Since the likelihood of two-body collisions is proportional to the atomic density ρ^2 , this leads to a much smaller effect of interactions in DFGs.

A widely used technique for enhancing interaction effects in DFGs is Feshbach resonances. A Feshbach resonance occurs between two species (either atomic species or spin species of the same atom) when the open channel, i.e. the two particles

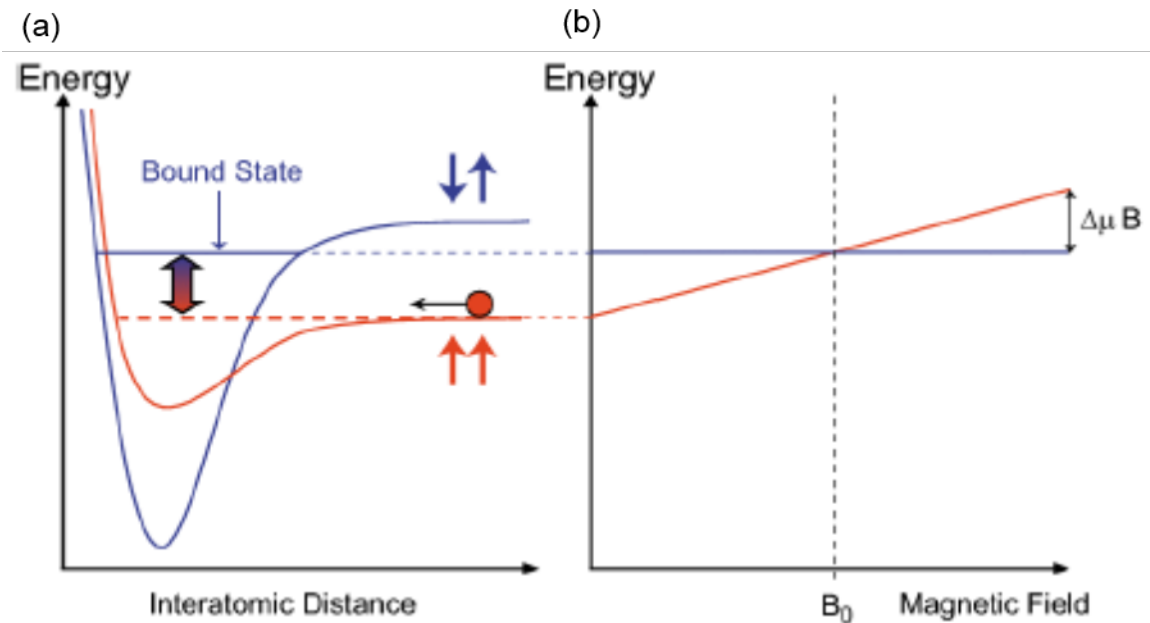


Figure 5: Schematic of a Feshbach resonance. (a) Pictoral representation of energy as a function of interatomic distance for an open channel (red) and closed channel (blue). (b) Energy as a function of background magnetic field B for the closed (blue) and open (red) channels. The energies coincide at the Feshbach resonance point B_0 . Energy of Figure taken from [15].

independently in their external potential, energetically approaches a closed channel, i.e. a bound molecular state of the two species, shown schematically in Figure 5a.

Generally, the atoms in an open channel are energetically sensitive to a background magnetic field \mathbf{B} via the hyperfine interaction $H_B = -\mu \cdot \mathbf{B}$, where μ is the magnetic dipole moment. Tuning the magnetic field should therefore tune the energy of the open channel. The molecular bound state may also have an overall magnetic moment, but it is generally not identical to that of the two atoms in the open channel, and therefore varies differently with the background field. Figure 5b shows an example where the bound state has zero magnetic moment. Here, the energy of both the closed and open channel as a function of background magnetic field \mathbf{B} is plotted in the vicinity of a Feshbach resonance. The resonance occurs at a field magnitude B_0 where the energies of the two channels coincide.

Assuming there is at least infinitesimal coupling between the closed and open

channels, as the energies of the two channels approach each other the perturbative correction term to the energy grows and the interaction between the atoms is affected. This is most easily seen in the *s*-wave case through changes in the scattering length a . In the case where there are no inelastic two-body channels, such as for the ${}^{40}\text{K}$ resonance discussed in this thesis, the interatomic scattering length as a function of background field is given by [16]

$$a(B) = a_{\text{bg}} \left(1 - \frac{\Delta}{B - B_0} \right), \quad (3.26)$$

where a_{bg} is the background scattering length, Δ is the width of the resonance, and B_0 is the field value at which the resonance occurs. The scattering length diverges at the resonance.

The tunability of interactions provided by Feshbach resonances has allowed for creation of molecular Bose-Einstein condensates from Fermi gases [17–19] as well as observation of the phase transition from the Bardeen-Cooper-Schrieffer (BCS) superconducting regime to the BEC regime at sufficiently low temperatures [20–23].

3.3 RbK apparatus

The rubidium-potassium (RbK) apparatus at NIST Gaithersburg has been previously detailed in [10, 24, 25]. In this thesis, we will give a brief overview of the apparatus and how it is used to produce BECs of ${}^{87}\text{Rb}$ and DFGs of ${}^{40}\text{K}$, and only give detailed documentation for those parts of the apparatus that differ from previous works.

A photograph of the main experiment is shown in Figure 6. This is mounted on an optical table, with the science chamber elevated above the surface of the table. The atoms start at the ovens (off to the right, not in the photograph) and travel down the Zeeman slower until they are trapped in the science chamber. The

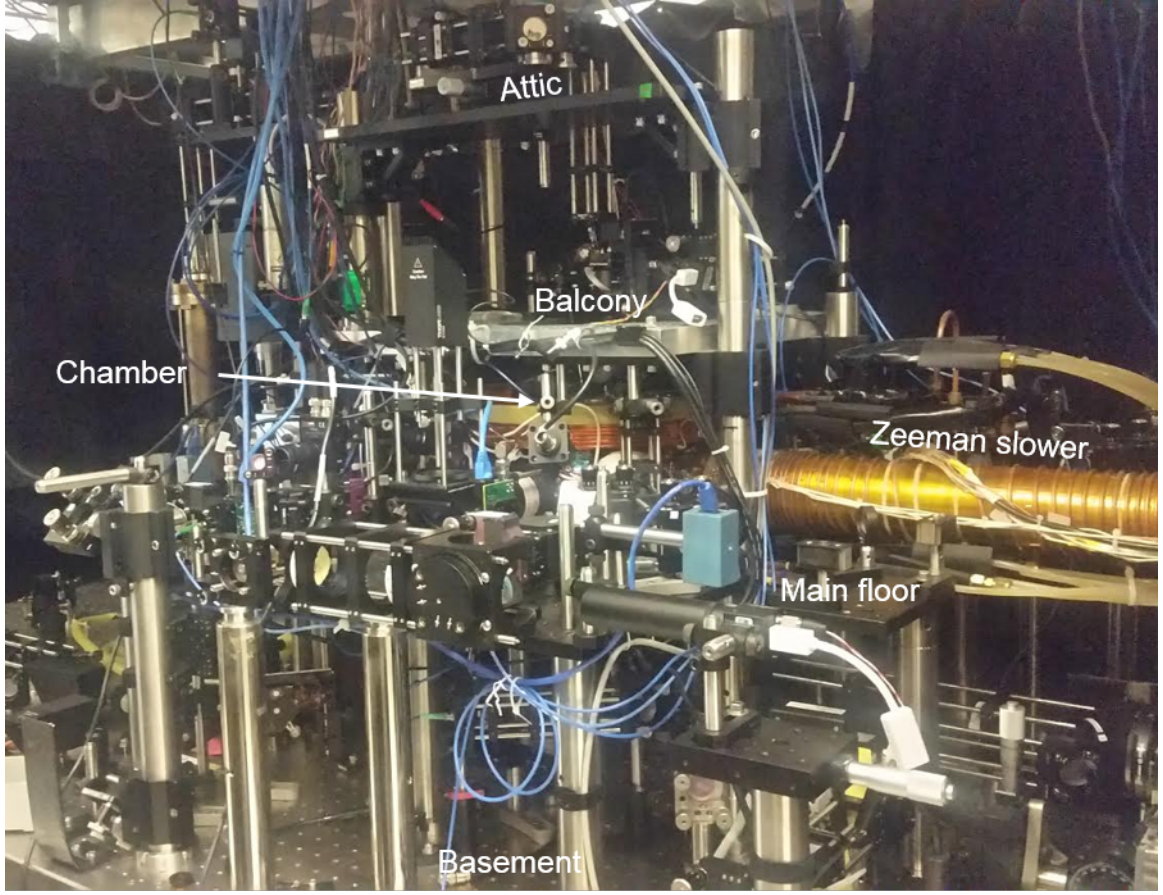


Figure 6: Photograph of RbK apparatus at NIST Gaithersburg. The main science chamber is at the center, hidden behind optics and coils. The Zeeman slower connects the atomic ovens (not shown) to the chamber. There are several levels of breadboards on which optics are mounted, labelled here as basement (surface of optical table), main floor, balcony and attic.

optical dipole trap laser, as well as the 1-D optical lattice laser, are located on the optical table and coupled into optical fibers, which are output on the main floor of breadboard before being sent towards the atoms. All other lasers are located on other optical table and brought over to the experiment table via optical fibers.

3.3.1 Laser beams

Figure 7 details the beam paths of the light going through the atoms. Figure 7a shows a side view of the apparatus. The up and down going MOT cooling beams

are shown in red, reaching the atoms when the flipper mirrors M_{top} and M_{bottom} are flipped in. The down going probe beam, used for imaging along the $x - y$ axis both in situ and in time-of-flight, is shown in solid blue. The probe beam is split via a polarizing beam splitter cube to allow for both in situ and time-of-flight imaging of the same cloud, shown in the inset in fig. 7b and described in greater detail in sec. 3.3.4. The dashed blue line represents the upward going probe beam introduced for alignment purposes, described in greater detail in sec. 3.3.4. The kinematic base mirror (green in the figure) is removable, and only inserted when the alignment beam is in use.

Figure 7b show's a bird's eye view of the apparatus, with optics on the main floor breadboard. The slower cooling (solid dark blue) and slower repump (dashed dark blue) are coming in from the left to slow the atoms as they are moving through the Zeeman slower. The remaining four MOT cooling beams, coming from four opposing directions, are shown in red. They reach the atoms when their flipper mirrors, $M1 - 4$, are flipped in. All six flipper mirrors are computer controlled by the same digital channel, so they can be flipped in and out together. Only the beams going in through mirrors $M1$ and $M2$ are accompanied by MOT repump light, dashed red lines. The repump light for ^{87}Rb (both MOT and slower) comes from a Toptica DL-100 laser. The cooling light (MOT, slower) as well as imaging beams, come from a Toptica TA-100 tapered amplifier system. Both lasers are frequency referenced to a master laser, a toptica DL-pro, which is frequency stabilized to a ^{87}Rb atomic transition via saturated absorption spectroscopy (see section 3.3.4).

The optical dipole trap beams (solid green) come from the same 1064 nm laser (IPG YDL-30-LP), and are split via an acousto-optic modulator into two orders, which enter from opposite directions and intersect each other at approximately a 90 degree angle, providing confinement along all three axes. There is a 1-D optical lattice beam (dashed green), also 1064 nm (IPG YAR-10K-1064-LP-SF, seeded by

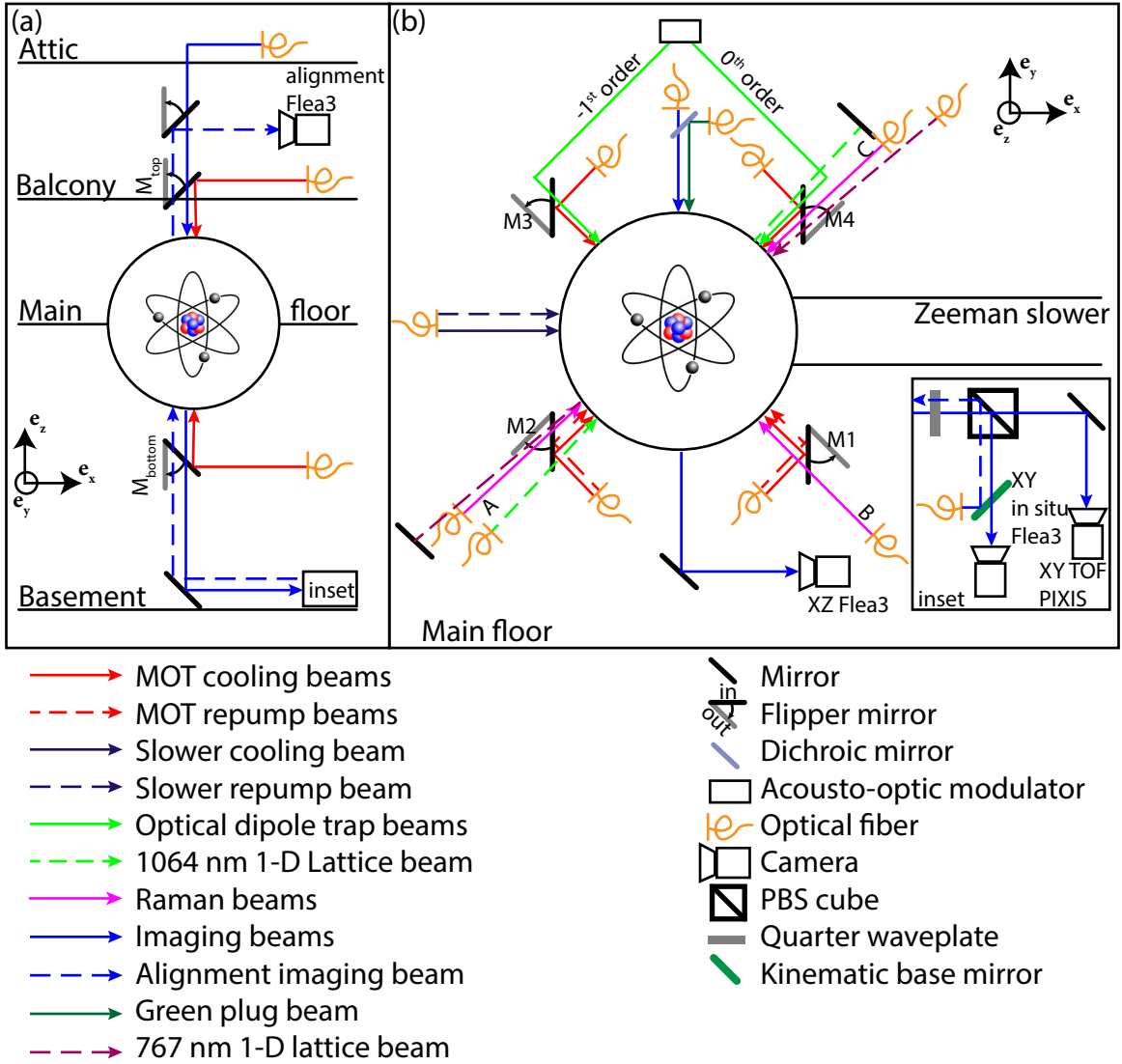


Figure 7: Schematic of RbK apparatus. (a) Side view of apparatus. Only beams propagating along the e_z direction through the atoms are pictured. (b) Top view of apparatus. Only beams propagating along the x - y plane are shown. Schematic is not to scale and the angles are approximate.

a pick off from an NP Photonics seed laser), sent in past the $M2$ mirror and retro-reflected on the opposite end of the chamber to form a standing wave pattern. This was also used for experiments in Chapters ???. There is also another imaging beam, imaging the atoms along the x - z plane, going to a Flea3 camera.

There are three Raman beams (solid magenta): Raman A, entering past the flipped-out $M2$ mirror, Raman B, at 90 degrees to Raman A entering past the $M1$ mirror, and Raman C, counter-propagating with Raman A and entering past the $M4$ mirror. The Raman beams are derived from a tunable Coherent MBR-110 Ti:Sapphire laser seeded by a Coherent Verdi V-10 laser. For experiments described in Chapters ???, we used the Raman A and C beams.

When ^{40}K atoms are in use, the slower cooling, slower repump, MOT cooling, MOT repump and imaging beams are all a combination of frequencies for both ^{87}Rb and ^{40}K , fiber coupled before they were sent to the main experiment table. Both the ^{40}K cooling and repump lasers are Toptica TA-pro systems, with the repump laser frequency stabilized to the ^{40}K atomic transition. In addition, a green plug beam (solid dark green in 7b) is used (see section 3.3.5), derived from a Coherent Verdi V-5 laser. For ^{40}K experiments detailed in Chapter ??, we used a near resonant retroreflected optical lattice beam, shown in dashed dark magenta entering past the $M4$ flipper mirror, coming out past the $M2$ mirror before getting retro-reflected.

3.3.2 Magnetic coils

Figure 8 is a schematic depiction of all the coils used to produce magnetic fields on the RbK apparatus. The quad coils (orange in the figure) are a large pair of coils used to produce a quadrupole field for the MOT. The top and bottom coils are connected through four IGBT switches, forming an h-bridge (see Figure 4.9 in [25]). This allows switching between two configurations: anti-Helmholtz and Helmholtz. In anti-Helmholtz configuration, the top and bottom coils conduct current in op-

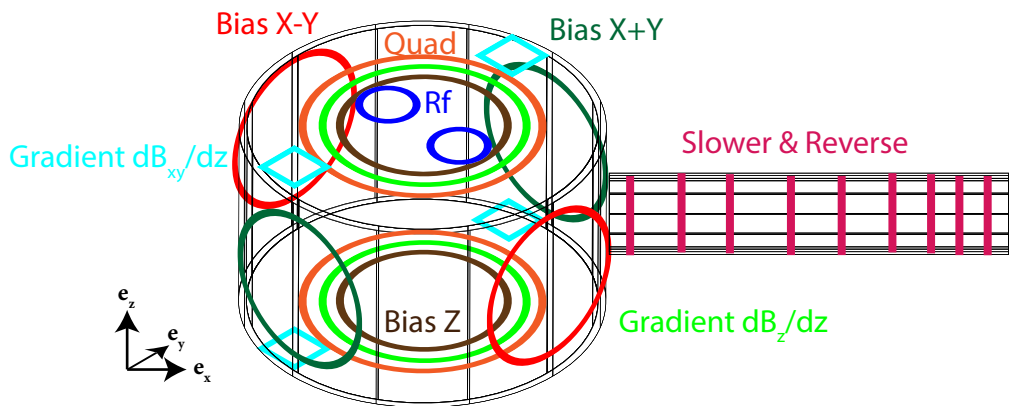


Figure 8: Schematic of magnetic coils on the RbK apparatus. The black wire frame represents the main experiment chamber, with the Zeeman slower off to the right. The Zeeman slower and reverse coils are wound around the Zeeman slower in varying spatial frequency (magenta). The quad (orange), gradient cancellation dB_z/dz (bright green) and bias Z (brown) are all pairs of identical coils on the top and bottom of the apparatus. Bias X-Y coils (red) are a pair of identical coils around the axes of the M_1 and M_3 mirrors, and the bias X+Y (dark green) are a pair of identical coils around the axes of the M_2 and M_4 mirrors. The rf coils (blue) are a pair of circular coils on top of the experimental chamber, spaced enough to allow the top MOT beam through. The gradient cancellation coils dB_{xy}/dz (cyan) are four square coils on top and bottom of the experiment along the X+Y axis.

posite directions, producing a quadrupole field gradient at the center. This is the configuration used for the MOT, as well as for producing a Stern-Gerlach gradient for spin resolved imaging. In Helmholtz configuration, the two coils conduct current in the same direction, producing a strong bias field along the e_z direction. This was used to get close to the Feschbach resonance in the experiment detailed in Chapter ??.

There are three pairs of bias coils, used to cancel constant background fields or provide field offsets along the three axes. All three are in Helmholtz configuration. The bias Z coils (brown) are on top and bottom of the experiment and provide a constant B_z field at the center. The bias X+Y coils (dark green) are vertical on two opposite sides of the apparatus along the $e_x + e_y$ directions, and the bias X-Y (red) are on the other two opposing sides along the $e_x - e_y$ directions. There are also two sets of gradient cancellation coils available, although they are not subject to feedback loops or computer control. The first is another pair of coils on top and bottom of the apparatus (bright green), connected in anti-Helmholtz configuration to produce a small gradient dB_z/dz . The second is four square coils mounted above and below each bias X+Y coil (cyan). Both vertically stacked pairs of coils are wound in Helmholtz configuration, and the two pairs are in series, providing a small gradient dB_{xy}/dz at the atoms.

3.3.3 Procedure for making a BEC

We begin with the atoms heated in the ovens, sent through a thin nozzle allowing only those atoms with a velocity towards the science chamber to enter. They are cooled via a Zeeman slower and captured in a Magneto-Optical trap (MOT) in the science chamber. During this step, the Zeeman slower is on, with both the coils and the slower cooling and repump lights on. These beams (dark blue in Figure 7b) are 7.6 MHz red detuned from the $|F = 2, m_F = 2\rangle$ to $|F = 3, m_F = 3\rangle$

transition of ^{87}Rb (for this, the cooling TA is locked to a 133 MHz beat note offset from the master laser). At the same time, the flipper mirrors $M1 - 4, M_{bottom}, M_{top}$ are flipped in and the MOT cooling and repump beams (red in Figure 7) are on. The quad coils are on in anti-Helmholtz configuration with 25 A of current running through them, producing a field gradient of $\frac{dB_z}{dz} \approx 13$ Gauss/cm. This step can be set to take anywhere from ≈ 0.7 s to ≈ 5 s depending on how many atoms are needed.

Next is the optical molasses step, during which sub-Doppler cooling of the atoms occurs. For this step, the Zeeman coils and slower lights are turned off. The quad coil current is also switched off, leaving just the MOT cooling light and only leakage MOT repump light. The MOT cooling light is set to 20.6 MHz below the $|F = 2, m_F = 2\rangle$ to $|F = 3, m_F = 3\rangle$ transition (120 MHz beat-note command). It is then linearly ramped in 19 ms down to a red detuning of 90.2 MHz (50 MHz beat-note command). Since the repump light is all but off in this step, the atoms are also depumped into the $F = 1$ manifold. Then, the atoms are optically pumped into the $|F = 1, m_F = -1\rangle$ state to make them trappable by the quadrupole field. This is done by turning on the slower repump beam (dashed dark blue in fig. 7b) 1 ms. Then, the XZ imaging beam (blue in fig. 7b) is briefly turned on to get rid of any remaining $F = 2$ atoms.

Next, we compress the atoms and perform forced rf evaporation. To compress, the quad coils are first turned on to 130 A. After holding for 20 ms, we sweep the current linearly to 250 A in 200 ms. The forced rf evaporation is then performed by turning on the rf coupling field and sweeping the frequency from 20 MHz to 4 MHz in 4 s to couple the highest energy atoms from $|F = 1, m_F = -1\rangle$ to $|F = 1, m_F = 0\rangle$ and allow them to escape the trap. The slow ramp is designed to allow the system to rethermalize through collisions as the hottest atoms are ejected. During rf evaporation, the crossed optical dipole trap (ODT) is on at an initial command power of

2.0 V and initial split (command to AOM controlling the power split between the two crossing beams, shown in fig. 7b) of 0.01 V. This allows any atoms that are cold enough to see the optical trap to be captured by it.

Then, the atoms are decompressed and loaded into the ODT. The quad current is ramped down to 60 A exponentially with a time constant of $\tau = 1.5$ s in 3 s. This is the quad current at which the atoms are only barely suspended against gravity by the quadrupole trap. At the same time, the bias Z current is ramped down from 10 A to 8 A, lowering the center of the quadrupole trap to the ODT. Then, the atoms are further evaporated in the ODT. This is done over the course of 5 s, ramping down the depth of the ODT and allowing the hottest atoms to escape. During this step, the ODT power is ramped exponentially from the initial command of 2.0 V to a final command of 0.4 V, while the split command is ramped up linearly from 0.01 V to 0.65 V, effectively turning on the crossing -1^{st} order beam. It is during this evaporation step that the atoms are cooled below the critical temperature and Bose condense.

Finally, the quad current is ramped exponentially to 0 A in 5 s, leaving the atoms optically trapped. Then any desired experiment can be performed on the BEC. For daily checks of the BEC, no experiments are performed and the atoms are released from the trap and allowed to expand in time-of-flight for 16.2 ms before being absorption imaged in the XY plane by the PIXIS imaging camera, pictured in fig. 7b.

3.3.4 Changes to apparatus for Rubidium

In this section, we describe a few of the changes that were made to the apparatus since the writing of Lauren Aycock’s thesis [25]. This is not an exhaustive list, but rather the most notable changes to the main setup affecting BEC production or adding capabilities to the apparatus.

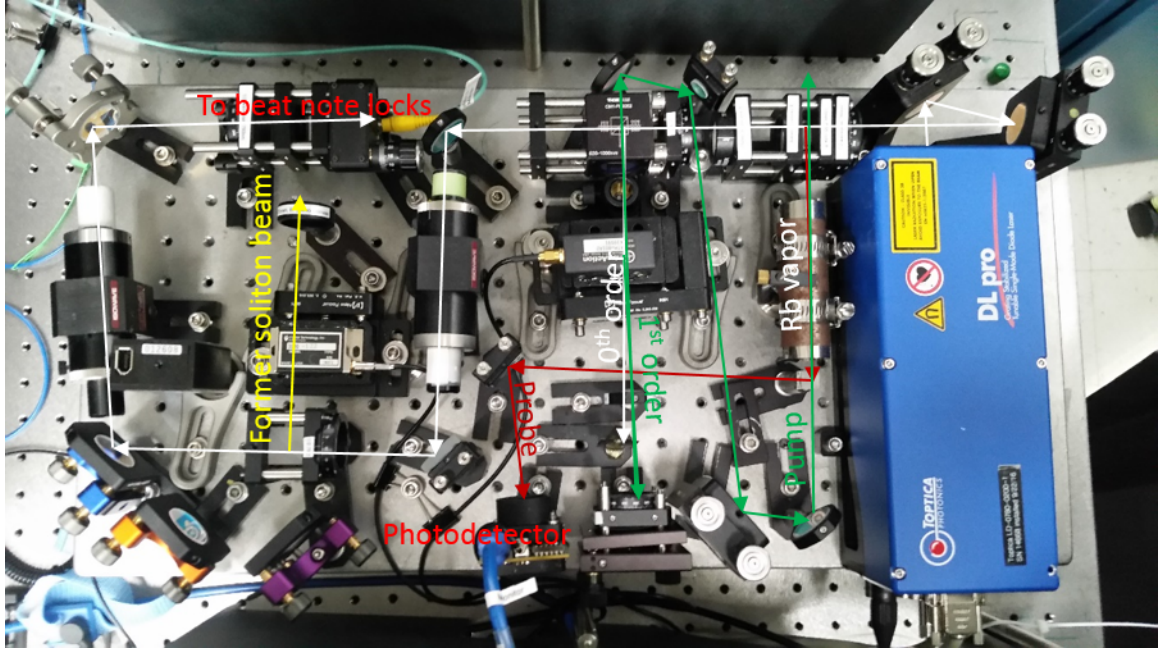


Figure 9: New master board layout.

3.3.4.1 Master laser setup

In 2014, the master laser board was replaced by a new version, with a new laser that was not dying. The laser was a Toptica DL-Pro, and it output approximately 80 mW, allowing for an extra beam arm that was used to imprint a phase shift on half the cloud to produce a soliton in the soliton project [ADD REFERENCE TO POINT IN THESIS HERE] [26].

The layout of the new master laser board is shown in Figure 9. The board contains saturated absorption spectroscopy to lock the laser frequency relative to the atomic resonance, an output port to send to the cooling and repump lasers for beat note locking and monitoring purposes, and an output port (partially dismantled in the figure) for any use if necessary. There are two mirrors directly in at the laser output, for easy re-alignment of the whole board if a diode is changed or other internal laser adjustments are made.

After hitting the two mirrors, the beam is used for saturated absorption spec-

troscopy, as described in section 8.3 of [27]. It is first split into two branches by a polarizing beam splitter cube (PBS). The power split between the branches can be adjusted by a half wavplate (HWP) preceding the PBS. One branch is used as the probe beam in saturated absorption (red in the figure). This branch goes through the Rb vapor cell and is then sent to a photodetector. The photodetector reading is sent to a scope for monitoring and to a lock-in amplifier, used to derive the error signal for frequency locking. The rest of the beam (white) then hits another PBS cube (again preceded by a HWP to control the power split), splitting off the pump beam (green) for saturated absorption spectroscopy. This beam is sent to an acousto-optic modulator (AOM). This AOM's frequency is modulated by the lock-in amplifier [LOOK UP RELEVANT NUMBERs]. The 0th order out of the AOM is blocked by a razor blade. The 1st order is retro-reflected in a cat's eye configuration [28]. Note that after retro-reflection, the second pass through the AOM also produces a 0th and 1st order beam. This 0th order beam is not blocked, but continues along the 1st order (pump beam) path at a slightly different angle - care must be taken to avoid aligning this order to counter-propagate with the probe. The double-passed beam (1st order in both directions, frequency shifted up twice) is then used as the pump and sent through the Rb vapor cell in the opposite direction of the probe beam.

The rest of the laser beam (white) then goes through an optical isolator, to avoid any subsequent reflections off of fiber tips or anything else from disturbing the saturated absorption frequency lock. Then, the beam hits another HWP followed by a PBS, splitting off the former soliton beam (yellow). In the figure, the soliton beam launch has been partially dismantled, but can be revived at any moment if needed. The beam was double-passed through an AOM in a cat's eye configuration before being sent into a fiber launch. The rest of the laser power (white) is sent into a fiber that is connected to a fiber splitter box, providing light for beat note locking

of the ^{87}Rb repump and cooling lasers as well as for monitoring the master laser on a wavemeter and Faby-Perot cavity.

3.3.4.2 Alignment imaging path

In 2016, there was a plan to carry out a project to create a 1D magnetic lattice whose topological character flips in the middle of the lattice, predicted to support localized states at the boundary. For this, two Raman beams needed to be overlapping, with one having a sharp phase change centered on the atoms. This required precise control of the beam phase as well as precise alignment of the beam center to the atoms. For optimal resolution, the Raman beams were to be sent upwards through the XY imaging system. To aid in alignment, it was decided that an additional imaging path that could detect these Raman beams directly be built. This alignment imaging path was implemented by Dr. Hsin-I Lu and is outlined in this section. All figures in this section were made by Hsin-I Lu.

The bottom part of the setup, with optics on the basement level of the experiment optical table, is diagrammed in Figure 10. One of the Raman beams, here called RamanC, first hit a spatial light modulator to imprint a phase jump. RamanC is then combined with a second beam, here called RamanD, on a PBS. Both overlapped beams are sent backwards through the XY imaging system and up towards the atoms. The dichroic filter allowed the Raman beams ($\lambda \approx 790$ nm) to be reflected while the imaging light ($\lambda \approx 780.24$ nm) passed through to the imaging cameras. The beam for alignment imaging is sent up to the atoms backwards along the XY imaging beam path. It entered the path via a mirror on a kinematic mount, which could be removed to allow imaging through the usual camera focused in situ in XY (see Figure 7).

To set up an alignment imaging system going upwards through the chamber, it was necessary to insert a new imaging lens above the chamber, as close to the

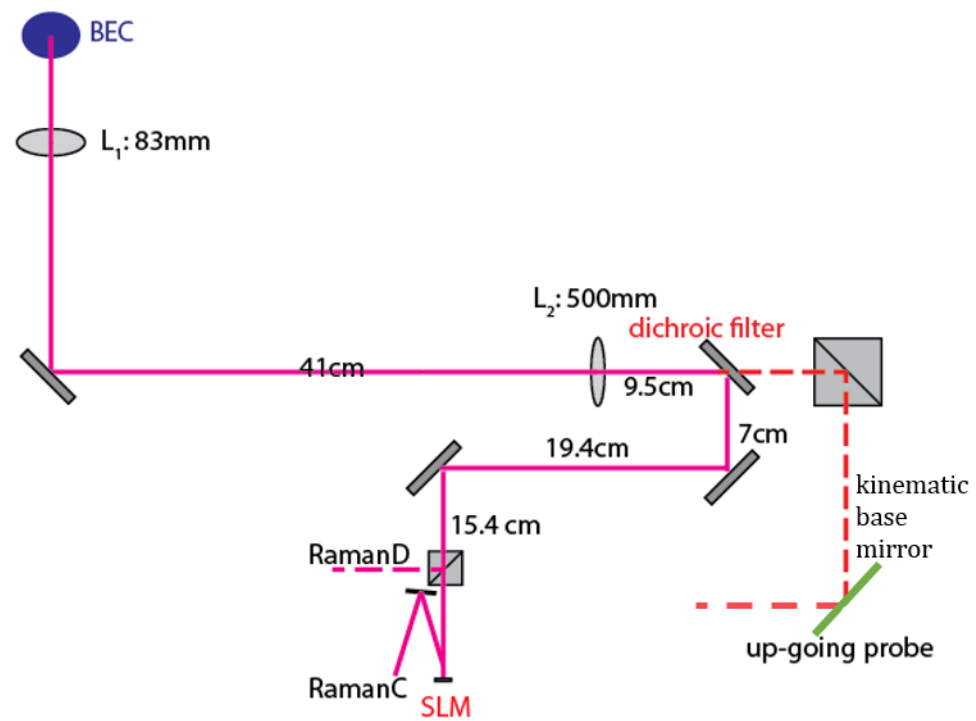


Figure 10: Schematic of the bottom half of the alignment imaging system, as well as the Raman beam set-up.

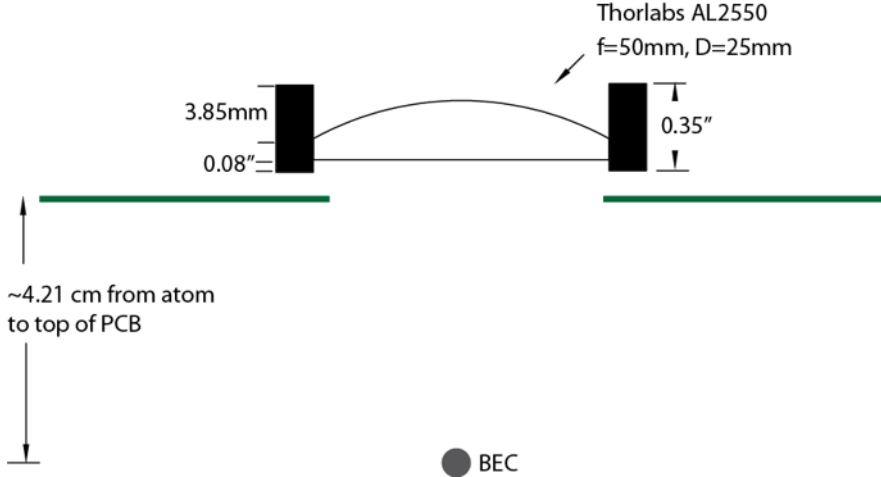


Figure 11: Schematic of the new imaging lens placed on the bucket window on top of the experimental chamber.

atoms as possible to maximize the numerical aperture. A schematic of this lens is shown in Figure 11, it is a 25 mm diameter $f = 50$ mm aspheric lens, a Thorlabs AL2550. This lens was placed above the printed circuit board (PCB) that contains the top bias Z coil and rf coils. It was held in a custom made mount.

The top part of the imaging system is diagrammed in Figure 12. Here, the alignment probe beam is light blue. From the atoms, the alignment probe beam hits the new imaging lens (labelled L_1). Then, if the top MOT mirror is flipped out, it hits another additional flipper mirror (here M_2) before reaching a second lens and hitting an additional Flea3 camera, on the 'balcony' level of the experiment. Since the imaging lens on top of the chamber cannot be taken in and out, it was necessary to correct the down-going probe beam and down-going MOT beam, ensuring they retain their size at the atoms. For the down-going probe beam, this was done by installing a telescope to expand the beam by a factor of 4 (L_6 and L_5 in the figure) and then add a lens (L_4 in the figure) that forms a telescope with the imaging lens to reduce the beam back down by a factor of 4. The MOT beam was corrected by switching the focusing lens directly after the MOT fiber to an $f = 100$ mm lens (L_7), effectively expanding the beam by a factor of $\approx 2/3$, and then adding an $f = 75$

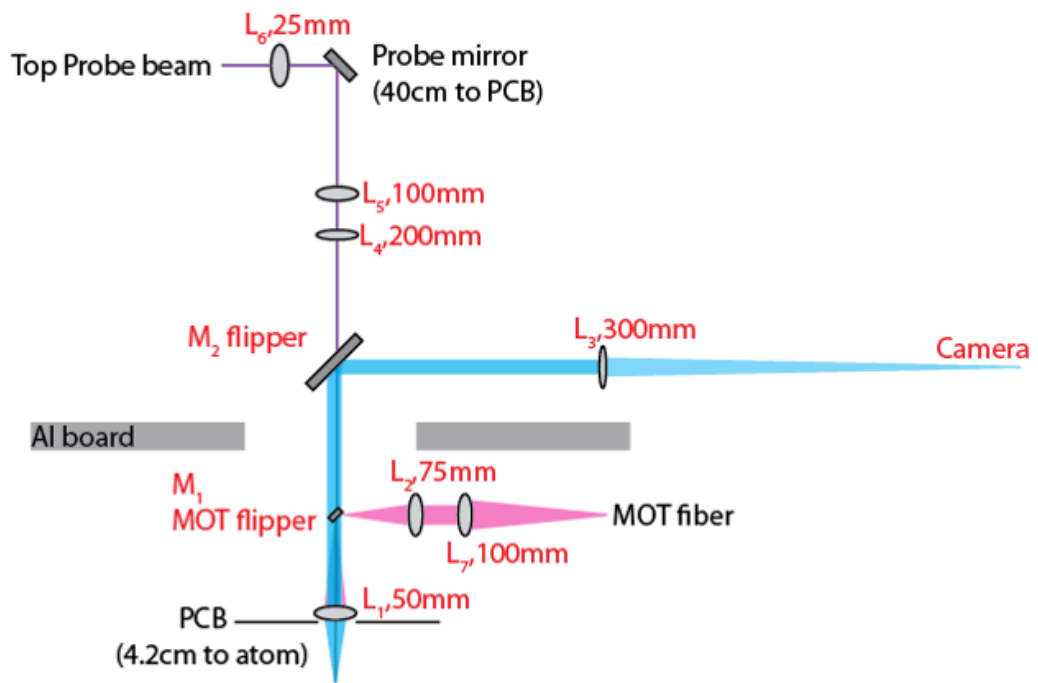


Figure 12: Schematic of the top half of the alignment imaging system, including correction optics for the MOT beam and probe beams to undo the effects of the new imaging lens.

mm lens (L_2) to form a telescope with the imaging lens, reducing the beam size by a factor of 2/3. The adjusted beams were aligned and the experiment functioned properly. The alignment imaging system was also aligned with great effort.

3.3.4.3 FPGA quad servo

In 2014, the servo board that was used to stabilize the current in the quad coils had failed, and rather than replacing it with an identical one a new FPGA-based servo board design by Ryan Price was implemented. This design is described in detail in Appendix B of [29]. Here, we include a brief description of the design and implementation details for the quad servo at RbK.

The basic operation of the board is as follows. There are four SMA connections for input signals. These signals go to a 16 bit, 8 channel analog to digital converter ADAS3022BCPZ, then through a digital isolator Si8662BC-B-IS1, to the FPGA board. The outputs of the FPGA are sent through a similar digital isolator, Si8660BC-B-IS1 and into a 16 bit, 4 channel digital to analog converter AD5686R. Then, each of the four outputs is sent through a programmable gain amplifier AD8250ARMZ. The gain setting signal is derived from the FPGA board , by way of a serial shift register CD74HC4094. There are four SMA connections for outputs of each of the four amplifiers.

All of these devices are powered from a +/-18 supply voltage by way of three voltage regulators, LM2940C_KTT_3 for 5V regulation, LM2990_KTT_3 for -15V regulation, and LM2940CSX_KTT_3 for +15V regulation. The FPGA communication is set up through USB. There is a USB input port that connects to a USB chip FT232HL. The USB chip requires an EEPROM, in this case 93LC56BT is used. Clock timing for both the FPGA and the USB chip is provided by CTX292-LVCT. There is also a buffer SN2564BCT25244 available for amplifying digital FPGA outputs. The digital side of the board is also powered from a separate 5V supply by

way of a 3.3V regulator LM1085_KTT_3.

For quad coil current stabilization, the board receives a computer command, in volts, through one of its input ports, and a Hall probe reading, in amps, through the other one. The Hall probe current sent to the servo is dropped across a stack of two 51 Ohm resistors for a total measured resistance of 25 Ohms. The difference between the two inputs, in volts, is interpreted as the error signal by the FPGA board. The control output of the board is then sent to the gate input of a MOSFET bank. The power supply powering the quad coils is connected to this MOSFET bank and then to the coils in series. Controlling the gate voltage of the MOSFETs controls the resistance the power supply sees and thus the current it outputs (in voltage limited mode).

The optimal PID parameters, set via software and programmed in the FPGA board, have been found at a gain factor of -5 and integrator bandwidth of 400 Hz. The resulting turn-on curve is shown in pink in Figure 13 a. For this curve, the computer command was hopped to 100 A and the resulting current as detected by the Hall probe was observed. The turn-on curve using the preceding servo board is shown in gray.

The board is also equipped with a digital TTL input (on the back of the board). When this digital input is high, the output control voltage is immediately railed to its lower bound. To be compatible with the MOSFETs used, the upper and lower bounds of the control output are set to 5 and 3 V respectively. The turn-off curve when this TTL switch is activated is shown in Figure 13 b. The timescale is likely limited by eddie currents in the chamber.

We calibrated the resulting current (as measured by the Hall probe) for different command voltages. This is shown in Figure 14. Both the schematic for the servo board and the Box control program to talk to the FPGA are in the shared google drive under 'RbK/Lab Notebook/Electronics/FPGA Quad Servo (From Ryan)'. When

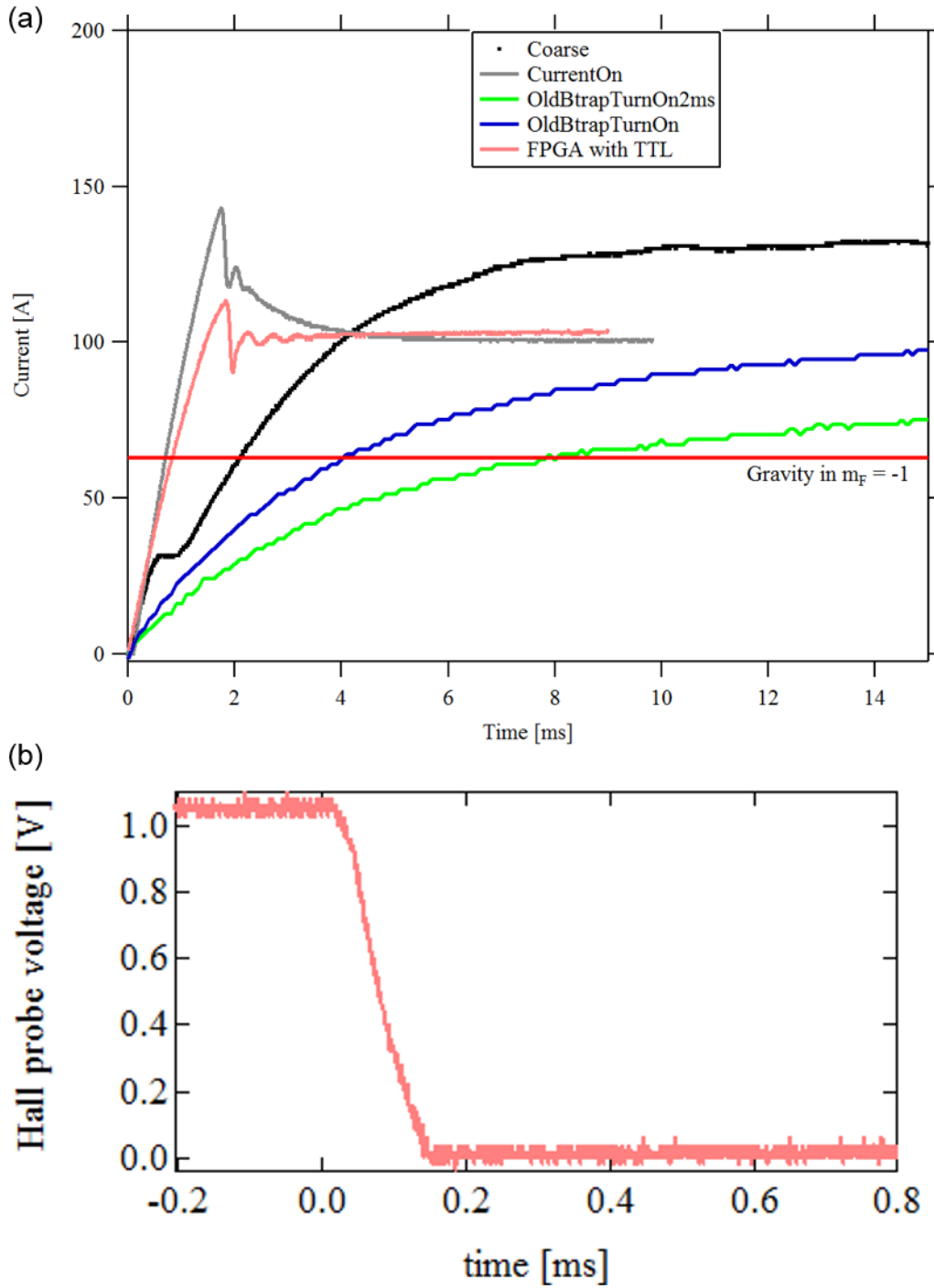


Figure 13: Turn on and off curves of the quad coils. (a) Turn-on, when computer command is jumped from 0 to 100 A . The FPGA-based servo response is in pink. The previous hardwired servo is in grey. The other curves are extraneous. (b). Turn-off with the FPGA-based servo when the TTL switch is engaged.

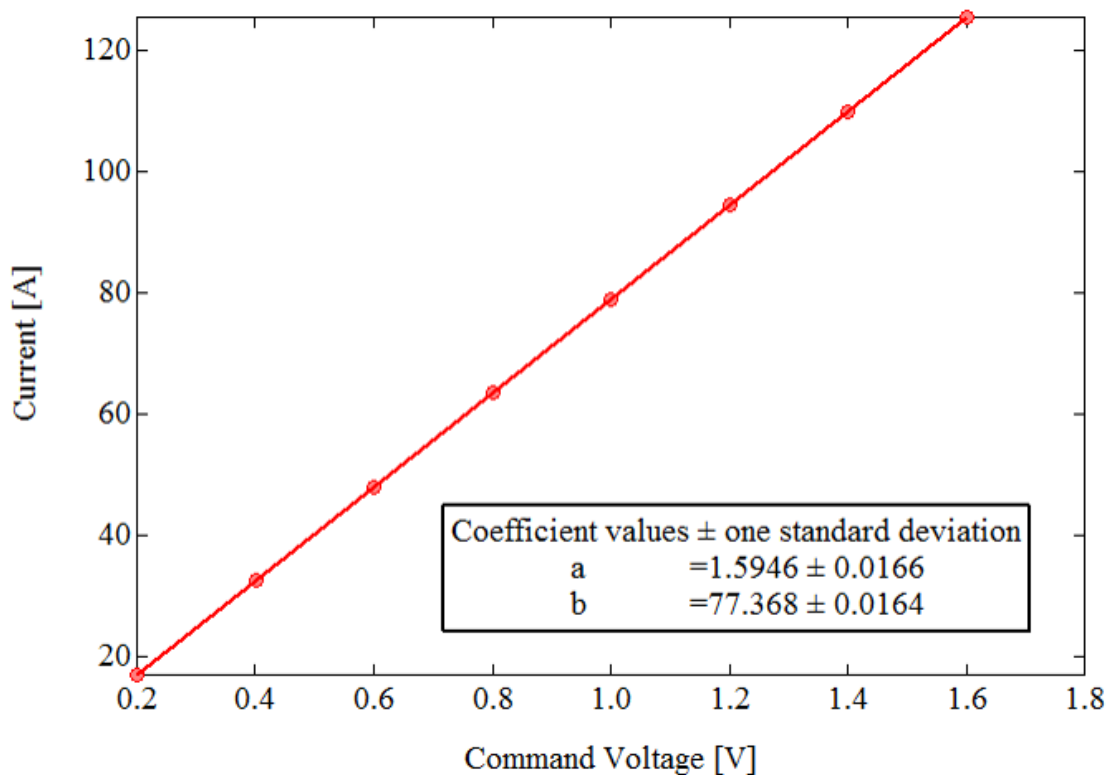


Figure 14: Output current as a function of computer command voltage for the FPGA-based servo implementation.

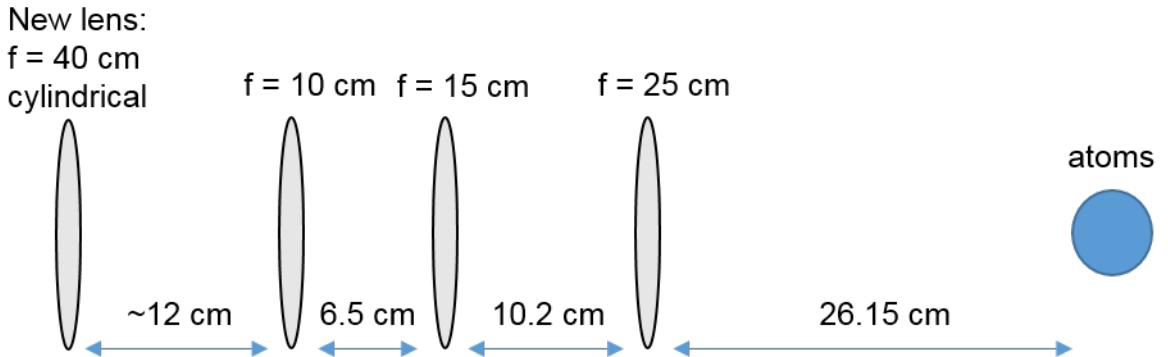


Figure 15: Schematic of beam shaping optics in the path of the 0th order ODT beam, after the split AOM. The new lens, on a removable mount, is cylindrical, shaping the beam along the horizontal axis only.

connected, the box control program detects 'RbK Quad Servo' in its device list. In the past, several cycles of plugging and unplugging as well as turning on and off have been necessary for the connection to be successfully made.

3.3.4.4 ODT beam shaping

In 2015, two projects were being carried out on the apparatus at the same time: the soliton project [PUT REFERENCE TO PAPER IN APPENDIX HERE] [26] and the synthetic dimensions project detailed in Chapter ???. The soliton project used an elongated BEC, requiring the dipole trap to be highly elongated along one direction, here $e_x + e_y$. For this, only the 0th order of the ODT was used and it was made very tight both along the horizontal and vertical directions: with 42 and 55 μm waists, respectively. The synthetic dimensions projects suffered from momentum changing collisions, and therefore needed the cloud to be as dilute as possible. For this, the 0th order ODT beam still needed to be tight in the vertical direction to suspend against gravity, but needed to be as wide as possible (while still retaining a detectable atom number) in the horizontal. Therefore, an extra cylindrical lens on a removable, rotatable mount was added in the beam path to switch between the two configurations.

The location of this new lens is detailed in Figure 15. Without this lens, the beam was sent through a telescope (the $f = 10$ and $f = 15$ cm lenses [DOESNT MAKE SENSE CHECK IF ONE IS DIVERGENT]) before reaching an $f = 25$ cm focusing lens, placed 25 cm away the center of the chamber to focus the beam at the atoms. The beam waist as a function of propagation distance along this beam path is shown in blue in Figure 16 a. This graph was made by Dr. Ian Spielman from a python calculation of gaussian beam optics. According to the calculation, the beam is focused down to a $45 \mu\text{m}$ waist at the atoms located at a displacement of 1400 mm.

The additional lens used was an $f = 40$ cm cylindrical lens, rotated in its rotating mount to focus the beam slightly in the horizontal direction. The effect of this lens on the horizontal beam waist along its path was calculated and plotted (again by Ian using his code) in Figure 16 b. This plot was made for a $f = 75$ cm lens instead of $f = 40$ cm, but the qualitative effect is the same. As seen in the figure, the waist of the beam is not significantly impacted by the addition of the lens, but the focus is shifte away from the atoms, resulting in a larger waist at the atoms. The horizontal beam waist at the atoms with the $f = 40$ cm lens as measured by a beam profiler camera was $115 \mu\text{m}$. This was the configuration used in the experiments described in Chapter 7.

3.3.5 Procedure for making a DFG

To make a degenerate Fermi gas of ^{40}K , we followed a similar cooling procedure as for making a BEC, with some key differences. First, as mentioned in sec. 3.2.2, due to the Pauli exclusion principle, spin polarized ^{40}K atoms cannot undergo *s*-wavecollisions, and therefore below a certain temperature have no method to thermalize on their own and cannot be evaporatively cooled. To overcome this problem, we cooled a mixture of ^{87}Rb and ^{40}K , effectively using ^{87}Rb as a collision mechanism

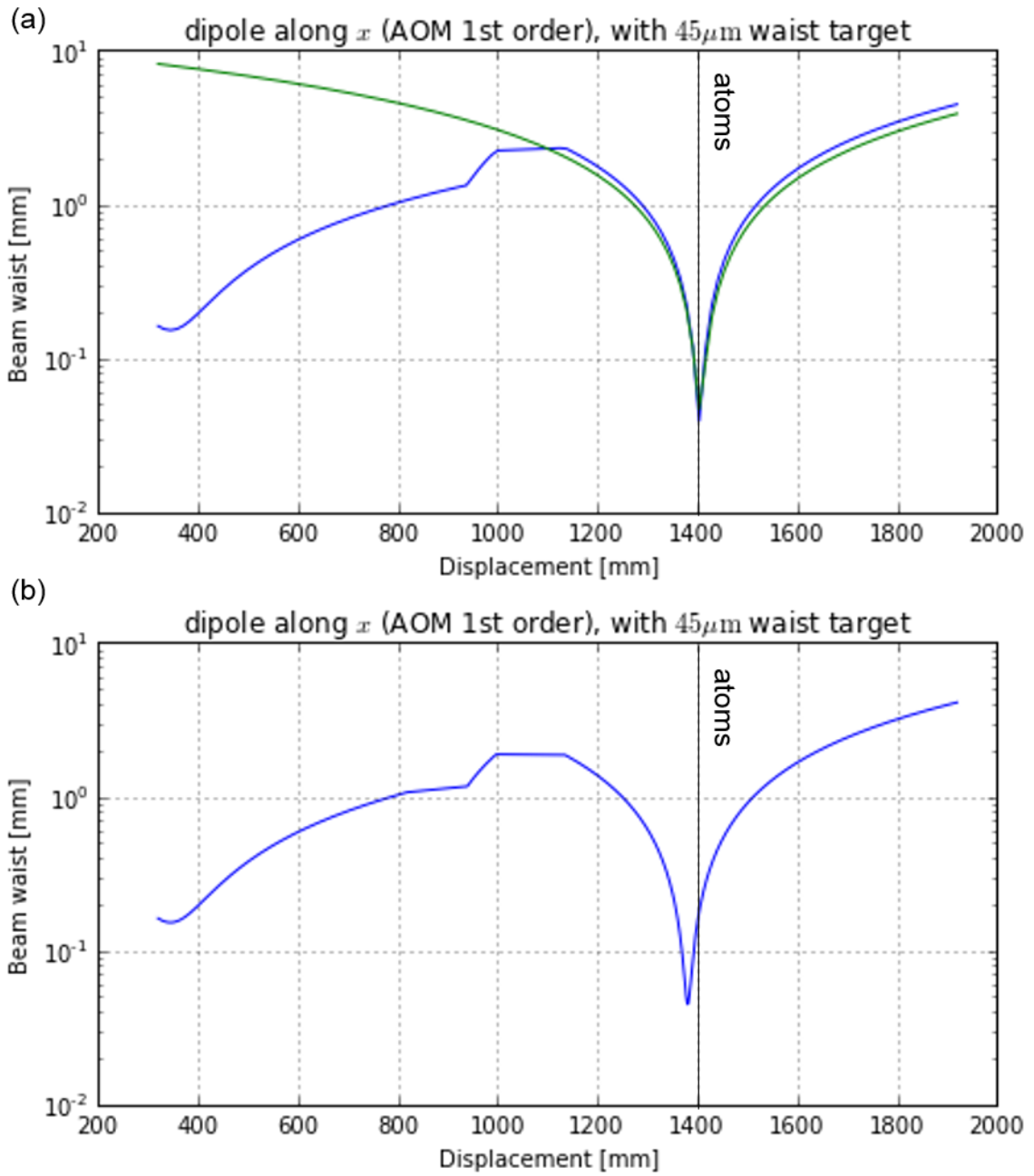


Figure 16: Beam waist as a function of propagation distance as calculated by Ian Spielman's code. Graphs also made by Ian Spielman. The atoms are at displacement = 140 cm. (a) Without additional lens. Blue line represents horizontal beam waist. (b) With an additional $f = 75$ cm lens 12 cm in before the next optic.

to allow the Fermions to thermalize. Second, ^{40}K is slightly below half the mass of ^{87}Rb . This leads to a larger magnitude of transverse velocity for ^{40}K atoms in the Zeeman slower, leading to a larger fraction of atoms missing the capture region of the MOT. To mitigate this issue, we utilized transverse cooling of ^{40}K before the Zeeman slower. This consisted of two pairs of counter-propagating beams along the $e_z + e_y$ and $e_z - e_y$ directions, performing Doppler cooling in the directions perpendicular to propagation (not shown in fig. 7b). The lower mass of ^{40}K also leads to a larger number of Majorana losses near the center of the MOT: spin flips that take the atoms out of the trappable states because they are moving too fast to adiabatically follow the changing magnetic field direction [30–32]. To mitigate this issue, for cooling ^{40}K the center of the quadrupole trap was plugged by a tightly focused green (repulsive) laser beam (dark green in fig. 7b).

First, ^{40}K atoms starting at the oven were cooled via a Zeeman slower and transverse cooling and captured in a MOT for 7 s. Then, both ^{40}K and ^{87}Rb atoms were slowed and MOT loaded for 1.5 s. The subsequent optical molasses step was only 2 ms long, with the ^{87}Rb MOT cooling light ramped linearly from -20.6 MHz below the $|F = 2, m_F = 2\rangle$ to $|F = 3, m_F = 3\rangle$ transition (120 MHz beat-note command) to -40.6 MHz away from resonance (100 MHz beat-note command). In this time, the ^{40}K cooling light was turned down in intensity but the detuning remained unaltered.

Next, ^{87}Rb was optically pumped into the $|F = 2, m_F = 2\rangle$ state using the slower cooling beam, while ^{40}K was optically pumped into the $|F = 9/2, m_F = 9/2\rangle$ state using a dedicated optical pumping beam in $250\mu\text{s}$. These are magnetically trappable states, and we subsequently turned on the quad coil current to 130 A to capture the atoms in the magnetic trap, along with the green plug beam at the center to prevent Majorana losses. Both species were compressed by a linear ramp of the quad current up to 160 A in 0.5 s. Then, forced rf evaporation was performed

for 10 s, sweeping the rf frequency linearly from 18 MHz down to 2 MHz.

Then, the atoms were decompressed and loaded into the ODT, similarly to the BEC procedure. The ODT was turned on to an initial power of 2 and an initial split command of 0.01. The quad current was ramped down to 25.5 A exponentially with a time constant of $\tau = 1.5$ s in 3 s. The evaporation in the ODT was split into two steps. During the first 3 s step, the split was ramped linearly to its final command power of 0.65, putting more power into the (less tightly focused) crossing beam. The green plug beam was ramped off during this step. During the second, 4 s step, the overall power of the ODT was exponentially ramped down to [CHECK THE INTERMEDIATE ODT COMMAND FOR K], while the quad coil current was ramped exponentially to 0.

We then used adiabatic rapid passage (ARP, see sec. 2.2.3) to transfer the ^{87}Rb atoms from $|F = 2, m_F = 2\rangle$ to $|F = 1, m_F = +1\rangle$ using a microwave coupling field and a 50 ms ramp in biasZ coil current. Then, we pulsed on the XZ imaging beam to eject any remaining $F = 1$ atoms. Then we performed one last evaporation step in the ODT, ramping the final power down to [CHECK THE FINAL ODT COMMAND FOR K]. The ^{87}Rb atoms were no longer suspended against gravity and fell out of the trap. We then were free to perform experiments with the degenerate ^{40}K cloud.

3.3.6 Current status of Potassium apparatus

At the time of writing, the ^{40}K part of the apparatus as described is no longer functional. The number of ^{40}K atoms collected in the MOT has started decaying significantly in January 2014, and by March was almost completely gone and could not be resurrected. The specific failure point of the setup was not clear. However, other groups have found that atomic sources are much more stable, and a higher fraction of the (expensive) ^{40}K sources can be utilized when the atoms were initially

cooled with a 2-D MOT rather than a Zeeman slower [33–35]. Therefore, rather than continuing to attempt to revive the existing set-up, the decision was made to build a 2-D MOT for both ^{40}K and ^{87}Rb .

The design of our 2D MOT is closely based on the design in Thomas Uehlinger's diplome thesis [34]. The design was developed by Dalia Ornelas, and initially implemented by Marcell Gall before it was taken over by the rest of the RbK team. The schemtaic of the planned vacuum system (with attached optics) is pictured in Figure 17. On the left side of the schematic, there are optics directing the pushing beam into a miniconflat viewport. The viewport is part of a cross, with the ^{40}K and ^{87}Rb ovens attached to the two ends of the cross, with gate valves allowing one to close off one or both sources from the rest of the vacuum system. From there, the cross attaches to the main 2D MOT cell via a mini-conflat flange.

The cell is a custom machined stainless steel frame with rectangular anti-reflection (AR) coated windows on four sides and mini-conflat conectors on two ends, pictured in more detail in Figure 18. Two aluminum mounting crosses attach two either end of the cell. Four aluminum bars are connected between the crosses, and the main 2D MOT optics are mounted on those four bars. The opposite end of the cell (right in fig. 17) sandwiches a differential pumping tube in the mini-conflat connection and connects to another cross. The top of the cross connects to a small ion pump. The bottom connects to a rotatable feed-through mechanism with a 'flag', a square of metal, attached inside. The rotator rotates the flag in and out of the atomic beam path, providing a means of losing off the main chamber from the atomic beam and push beam light. The fourth end of the cross connects to another gate valve, separating the 2D MOT vacuum system from the main experiment chamber. The other end of this gave valve connects to a flange that is meant to connect directly to the main experiment chamber.

A picture of the stainless cell is shown in Figure 18. Attaching the glass

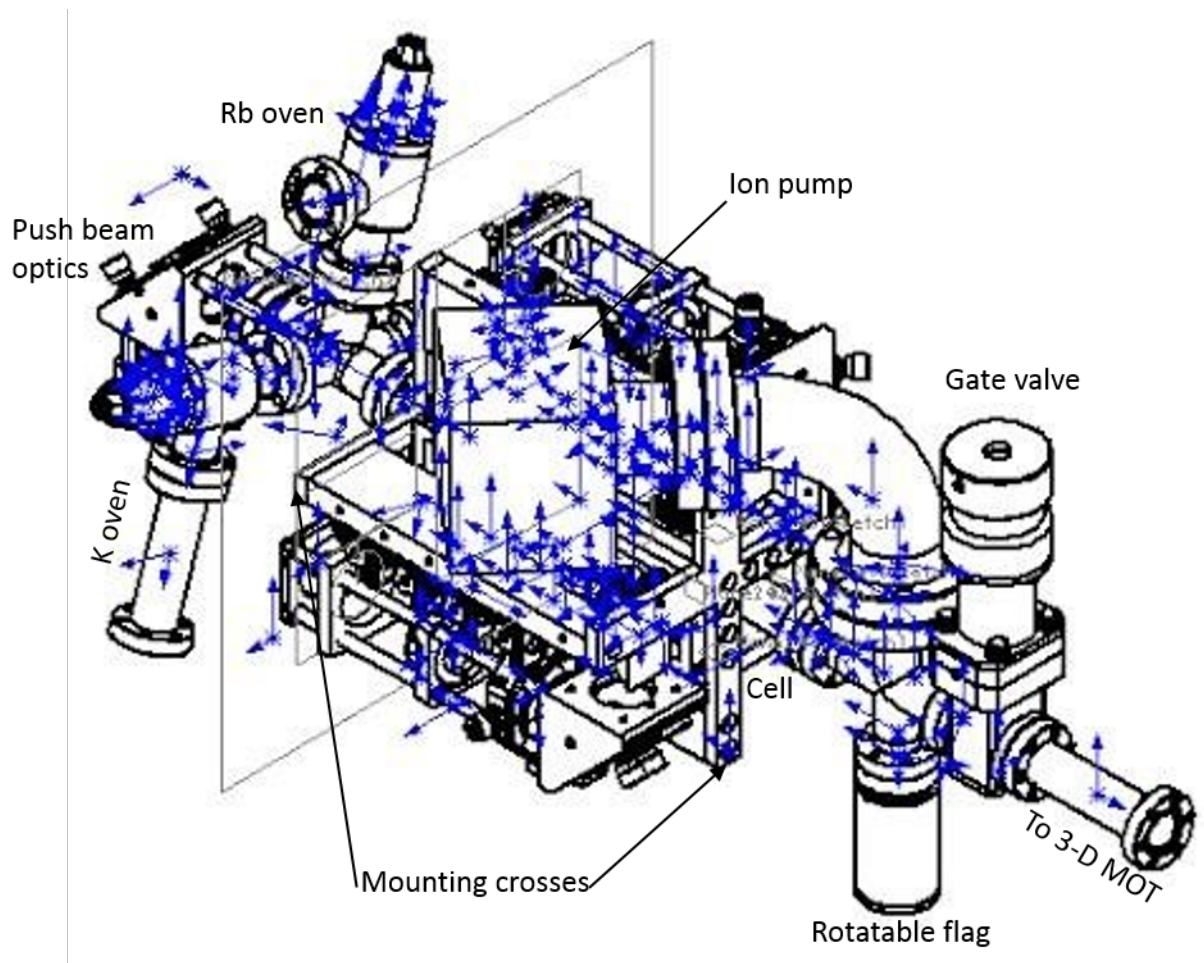


Figure 17: Schematic of the 2D MOT setup. The mini-conflat on the right is to be attached to the existing experiment chamber, directing the atomic beam into the 3D MOT.

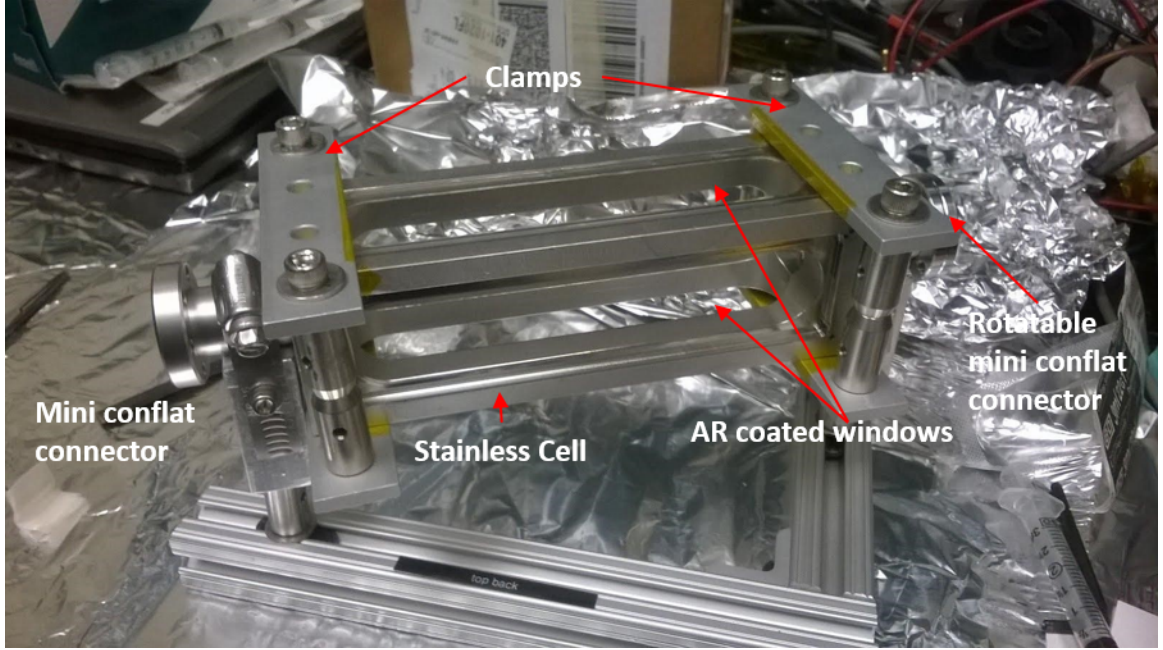


Figure 18: Picture of 2D MOT cell during an attempt to epoxy AR coated windows onto the stainless steel frame. The clamps serve to hold the windows in place while epoxy cures.

windows to the stainless steel frame in a vacuum tight way proved to be quite difficult, and this picture was taken during one of the attempts to do so using epoxy. The clamps around the cell served to keep the windows in place as the epoxy was curing. In the final design, the seal was made with indium, with gaskets custom machined to press the windows onto the cell. We roughly followed the indium sealing method presented in [36], with gaskets above and below the windows. We also employed pre-squashing, where a metal piece in the shape of the window was first pressed onto the indium wire to flatten it and minimize the amount of pressure that needed to be applied to the glass window.

The main 2D MOT optics direct the cooling and repump beams into the cell from two directions, and retro-reflect them on the other end, producing cooling along those two directions (hence the name 2D MOT). The optical set-up along one of those directions is presented schematically in Figure 19. The cell is elongated along the atomic beam direction, to maximize the time the atoms are cooled while

travelling to the 3D MOT. Because of this, instead of a highly elliptical cooling beam, four MOT beams are launched in a row, almost overlapping, from each of the two directions. This is accomplished by splitting one beam into four with four sequential beam-splitting cubes (BSs).

The 2D MOT cooling and repump light is first periscoped over from a fiber and lens assembly (designed to shape the beam to be roughly 1 inch in diameter). It then goes through a half-wave plate (HWP) before entering the first 70/30 beam splitter. 30% of the light is sent through a quarter-wave plate (QWP) tuned to provide circularly polarized light into the cell. On the other side of the cell, the beam hits another QWP before being retro-reflected back into the cell. Since the beam hits the QWP on the other side of the cell twice, the circular polarization is preserved. The remaining 70% of the light goes into the next 70/30 BS, sending 21% of the total beam power into the second arm going into the cell, to be retro-reflected in the same way. The remaining 49% hits a 50/50 BS, sending 25.5% of the total beam power into the third retro-reflected arm. The final cube is a polarizing beam-splitter (PBS), and the HWP before the cubes is tuned to ensure all of the light is sent into the cell on this last, fourth, arm.

The push beam enters from the oven direction and serves to provide some velocity to the atoms along the long direction of the cell to ensure they continue to travel to the 3D MOT, while still providing some cooling along the longitudinal direction. In order to provide this cooling, the push beam is also retr-reflected, with the help of a specially machined differential pumping tube (on the right in fig. 19). The differential pumping tube is machined to have a 45° angled polished end, reflecting all of the light except for the central part towards a retro-reflecting mirror outside the cell. Along the other 2D-MOT cooling direction (up and down in fig. 19), this whole set of optics is replicated, with the exception of the push beam retro-reflection.

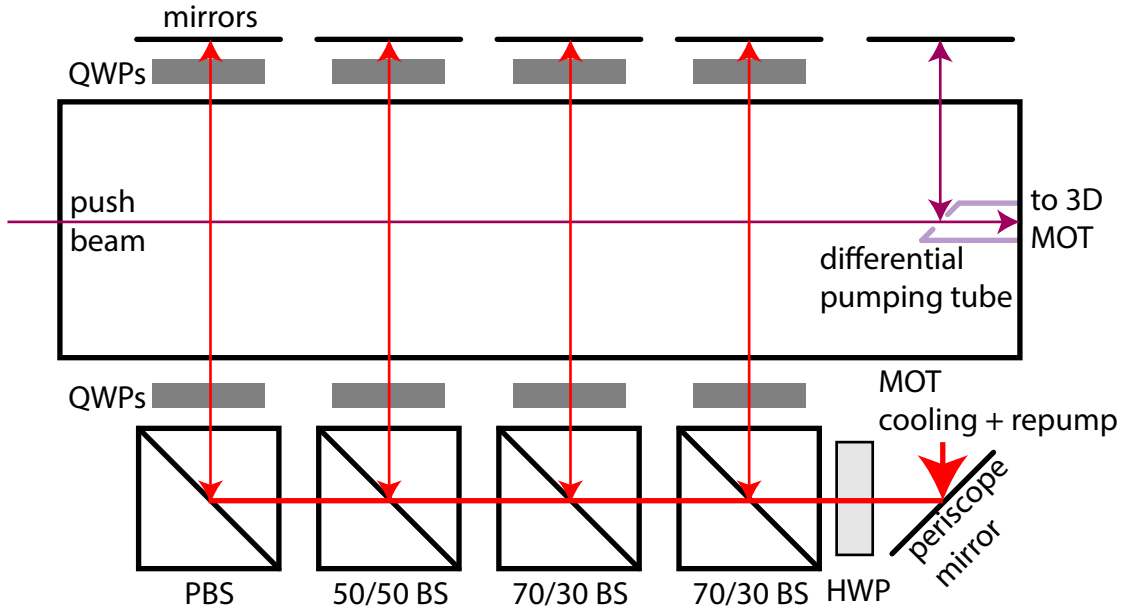


Figure 19: Schematic of 2D MOT optics along one direction. The main cooling and repump beam is split into four parallel arms by four beam splitter cubes. The push beam enters from the oven direction and is retro-reflected via a custom machined and polished differential pumping tube. These optics are mounted on crosses attached to the 2D MOT cell.

The current 2D-MOT setup is pictured in Figure 20. The vacuum system has been assembled and successfully pumped down, with a octagonal test chamber in place of the main experimental chamber. This test chamber is intended to be used to send probe light through and detect fluorescence to characterize the atomic beam coming out of the 2D MOT. The optics have been assembled and the quarter-wave plates lightly epoxied onto the BS cubes and mirrors, although as can be seen in the picture some have regrettably fallen off. Quadropole coils have been wound around each of the four windows, onto 3D printed coil winding forms. BiasZ coils have also been wound to cancel out stray gradients along the atomic beam direction.

The two Toptica TA-pro systems that were used to provide all ^{40}K light in the past are still operational, and need to be re-purposed to provide both 2D MOT and 3D MOT cooling and repump light. A new Toptica TA-pro was also purchased, with the intent to implement gray molasses cooling on the ^{40}K D1 line as described

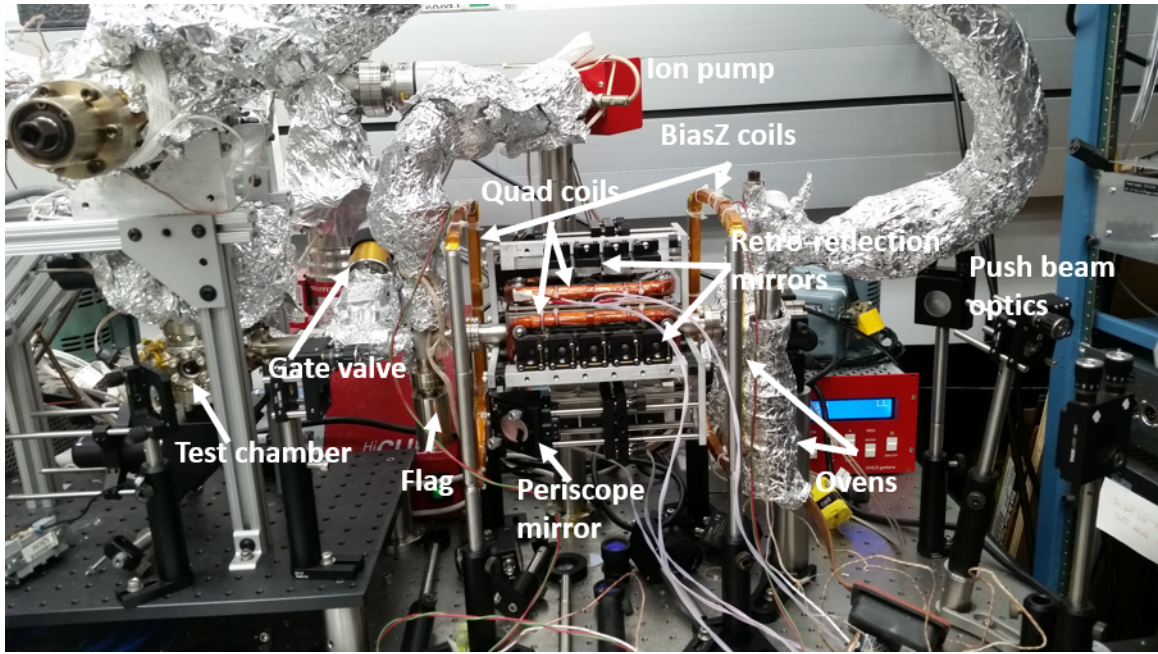


Figure 20: Picture of current 2D MOT apparatus. The vacuum system is in place, optics are (mostly) mounted and coils to generate the quadrupole trap and cancel gradients along the atomic beam direction have been wound.

in [37].

Bibliography

- [1] D. J. Thouless, M. Kohmoto, M. P. Nightingale, and M. den Nijs. Quantized hall conductance in a two-dimensional periodic potential. *Phys. Rev. Lett.*, 49:405–408, Aug 1982.
- [2] Xiao-Liang Qi and Shou-Cheng Zhang. Topological insulators and superconductors. *Rev. Mod. Phys.*, 83:1057–1110, Oct 2011.
- [3] Horst L. Stormer. Nobel lecture: The fractional quantum hall effect. *Rev. Mod. Phys.*, 71:875–889, Jul 1999.
- [4] N.W. Ashcroft and N.D. Mermin. *Solid State Physics*. Saunders College, Philadelphia, 1976.
- [5] Daniel Adam Steck. Rubidium 87 d line data. Available online, <http://steck.us/alkalidata>, April 2018. revision 2.1.5.
- [6] T. G. Tiecke. Properties of potassium. Available online, <http://www.tobiastiecke.nl/archive/PotassiumProperties.pdf>, May 2011. v1.02.

- [7] G. Breit and I. I. Rabi. Measurement of nuclear spin. *Phys. Rev.*, 38:2082–2083, Dec 1931.
- [8] H.J. Metcalf and P. van der Straten. *Laser Cooling and Trapping*. Graduate Texts in Contemporary Physics. Springer New York, 1999.
- [9] Nicola Marzari, Arash A. Mostofi, Jonathan R. Yates, Ivo Souza, and David Vanderbilt. Maximally localized wannier functions: Theory and applications. *Rev. Mod. Phys.*, 84:1419–1475, Oct 2012.
- [10] Karina Jimenez-Garcia. *Artificial Gauge Fields for Ultracold Neutral Atoms*. PhD thesis, Joint Quantum Institute, National Institute of Standards and Technology, and the University of Maryland, 2012.
- [11] K. Jiménez-García, L. J. LeBlanc, R. A. Williams, M. C. Beeler, A. R. Perry, and I. B. Spielman. Peierls substitution in an engineered lattice potential. *Phys. Rev. Lett.*, 108:225303, May 2012.
- [12] Daniel Adam Steck. Quantum and atom optics. Available online at <http://steck.us/teaching>, January 2015. revision 0.12.2.
- [13] C.J. Pethick and H. Smith. *Bose-Einstein Condensation of Dilute Gases*. Oxford University Press, Oxford, UK, 2005.
- [14] M. Egorov, B. Opanchuk, P. Drummond, B. V. Hall, P. Hannaford, and A. I. Sidorov. Measurement of s -wave scattering lengths in a two-component bose-einstein condensate. *Phys. Rev. A*, 87:053614, May 2013.
- [15] W. Ketterle and M. W. Zwierlein. Making, probing and understanding ultracold Fermi gases. In *Ultracold Fermi Gases, Proceedings of the International School of Physics ‘Enrico Fermi’, Course CLXIV*, Varenna, 20-30 June 2006.

- [16] C. Chin, R. Grimm, P. Julienne, and E. Tiesinga. Feshbach resonances in ultracold gases. *Rev. Mod. Phys.*, 82:1225–1286, 2010.
- [17] M. Greiner, C. A. Regal, and D. S. Jin. Emergence of a molecular Bose-Einstein condensate from a Fermi gas. *Nature*, 426(6966):537–540, 2003.
- [18] M. W. Zwierlein, C. A. Stan, C. H. Schunck, S. M. F. Raupach, S. Gupta, Z. Hadzibabic, and W. Ketterle. Observation of Bose-Einstein condensation of molecules. *Phys. Rev. Lett.*, 91:250401, 2003.
- [19] S. Jochim, M. Bartenstein, A. Altmeyer, G. Hendl, S. Riedl, C. Chin, J. Hecker Denschlag, and R. Grimm. Bose-Einstein condensation of molecules. *Science*, 302(5653):2101–2103, 2003.
- [20] M. Bartenstein, A. Altmeyer, S. Riedl, S. Jochim, C. Chin, J. Hecker Denschlag, and R. Grimm. Collective excitations of a degenerate gas at the bec-bcs crossover. *Phys. Rev. Lett.*, 92:203201, 2004.
- [21] T. Bourdel, L. Khaykovich, J. Cubizolles, J. Zhang, F. Chevy, M. Teichmann, L. Tarruell, S. J. J. M. F. Kokkelmans, and C. Salomon. Experimental Study of the BEC-BCS Crossover Region in Lithium 6. *Phys. Rev. Lett.*, 93:050401, 2004.
- [22] M. W. Zwierlein, C. A. Stan, C. H. Schunck, S. M. F. Raupach, A. J. Kerman, and W. Ketterle. Condensation of pairs of Fermionic atoms near a Feshbach resonance. *Phys. Rev. Lett.*, 92:120403, 2004.
- [23] C. A. Regal, M. Greiner, and D. S. Jin. Observation of resonance condensation of fermionic atom pairs. *Phys. Rev. Lett.*, 92(4), 2004.

- [24] Y.-J. Lin, A. R. Perry, R. L. Compton, I. B. Spielman, and J. V. Porto. Rapid production of ^{87}Rb bose-einstein condensates in a combined magnetic and optical potential. *Phys. Rev. A*, 79:063631, Jun 2009.
- [25] Lauren M. Aycock. *Topological excitations in a Bose gas and sexual harassment reported by undergraduate physicists*. PhD thesis, Cornell University, Ithaca, NY, 1 2017.
- [26] Lauren M. Aycock, Hilary M. Hurst, Dmitry K. Efimkin, Dina Genkina, Hsin-I Lu, Victor M. Galitski, and I. B. Spielman. Brownian motion of solitons in a bose-einstein condensate. *Proceedings of the National Academy of Sciences*, 114(10):2503–2508, 2017.
- [27] Christopher J. Fott. *Atomic Physics*. Cambridge University Press, Cambridge, UK, 2002.
- [28] E. A. Donley, T. P. Heavner, F. Levi, M. O. Tataw, and S. R. Jefferts. Double-pass acousto-optic modulator system. *Review of Scientific Instruments*, 76(6):063112, 2005.
- [29] Ryan Price. *Phase transitions in engineered ultracold quantum systems*. PhD thesis, University of Maryland College Park, Digital Repository at the University of Maryland, 6 2016.
- [30] E. Majorana. Atomi orientati in campo magnetico variabile. *Nuovo Cimento*, 9:43–50, Feb 1932.
- [31] C. V. Sukumar and D. M. Brink. Spin-flip transitions in a magnetic trap. *Phys. Rev. A*, 56:2451–2454, Sep 1997.
- [32] D. M. Brink and C. V. Sukumar. Majorana spin-flip transitions in a magnetic trap. *Phys. Rev. A*, 74:035401, Sep 2006.

- [33] J. Catani, P. Maioli, L. De Sarlo, F. Minardi, and M. Inguscio. Intense slow beams of bosonic potassium isotopes. *Phys. Rev. A*, 73:033415, Mar 2006.
- [34] Thomas Uehlinger. A 2-d magneto-optical trap as a high flux source of cold potassium atoms. Master's thesis, Swiss Federal Institute of Technology Zurich, Zurich, 5 2008.
- [35] E. Pedrozo-Peafiel, F. Vivanco, P. Castilho, R. R. Paiva, K. M. Farias, and V. S. Bagnato. Direct comparison between a two-dimensional magneto-optical trap and a zeeman slower as sources of cold sodium atoms. *Laser Physics Letters*, 13:065501, May 2016.
- [36] K. J. Weatherill, J. D. Pritchard, P. F. Griffin, U. Dammalapati, C. S. Adams, and E. Riis. A versatile and reliably reusable ultrahigh vacuum viewport. *Review of Scientific Instruments*, 80(2):026105, 2009.
- [37] D. Rio Fernandes, F. Sievers, N. Kretzschmar, S. Wu, C Salomon, and F. Chevy. Sub-doppler laser cooling of fermionic 40k atoms in three-dimensional gray optical molasses. *Europhysics Letters*, 100:63001, Dec 2012.
- [38] D. Genkina, L. M. Aycock, B. K. Stuhl, H-I Lu, R. A. Williams, and I. B. Spielman. Feshbach enhanced s-wave scattering of fermions: direct observation with optimized absorption imaging. *New Journal of Physics*, 18:013001, Dec 2015.
- [39] Lindsey J. LeBlanc. *Exploring many-body physics with ultracold atoms*. PhD thesis, University of Toronto, 2011.
- [40] E. Tiesinga, B. J. Verhaar, and H. T. C. Stoof. Threshold and resonance phenomena in ultracold ground-state collisions. *Phys. Rev. A*, 47(5, B):4114–4122, 1993.

- [41] M. Lysebo and L. Veseth. *Ab initio* calculation of Feshbach resonances in cold atomic collisions: *s*- and *p*-wave Feshbach resonances in ${}^6\text{Li}_2$. *Phys. Rev. A*, 79:062704, 2009.
- [42] B. Gao. Analytic description of atomic interaction at ultracold temperatures. II. Scattering around a magnetic Feshbach resonance. *Phys. Rev. A*, 84:022706, 2011.
- [43] S. Inouye, M. R. Andrews, J. Stenger, H. J. Miesner, D. M. Stamper-Kurn, and W. Ketterle. Observation of Feshbach resonances in a Bose-Einstein condensate. *Nature*, 392(6672):151–154, 1998.
- [44] S. L. Cornish, N. R. Claussen, J. L. Roberts, E. A. Cornell, and C. E. Wieman. Stable Rb-85 Bose-Einstein condensates with widely tunable interactions. *Phys. Rev. Lett.*, 85(9):1795–1798, 2000.
- [45] C. A. Regal and D. S. Jin. Measurement of positive and negative scattering lengths in a Fermi gas of atoms. *Phys. Rev. Lett.*, 90:230404, 2003.
- [46] K. M. O’Hara, S. L. Hemmer, M. E. Gehm, S. R. Granade, and J. E. Thomas. Observation of a strongly interacting degenerate Fermi gas of atoms. *Science*, 298(5601):2179–2182, 2002.
- [47] C. Monroe, E. Cornell, C. Sackett, C. Myatt, and C. Wieman. Measurement of Cs-Cs elastic scattering at $T = 30 \mu\text{K}$. *Phys. Rev. Lett.*, 70:414–417, 1993.
- [48] B. DeMarco, J. L. Bohn, J. P. Burke, M. Holland, and D. S. Jin. Measurement of *p*-wave threshold law using evaporatively cooled fermionic atoms. *Phys. Rev. Lett.*, 82:4208–4211, 1999.
- [49] S. Wu, Y.-J. Wang, Q. Diot, and M. Prentiss. Splitting matter waves using an optimized standing-wave light-pulse sequence. *Phys. Rev. A*, 71:043602, 2005.

- [50] M. Edwards, B. Benton, J. Heward, and C. W. Clark. Momentum-space engineering of gaseous bose-einstein condensates. *Phys. Rev. A*, 82:063613, 2010.
- [51] K. v. Klitzing, G. Dorda, and M. Pepper. New method for high-accuracy determination of the fine-structure constant based on quantized hall resistance. *Phys. Rev. Lett.*, 45:494–497, Aug 1980.
- [52] Douglas R. Hofstadter. Energy levels and wave functions of bloch electrons in rational and irrational magnetic fields. *Phys. Rev. B*, 14:2239–2249, Sep 1976.
- [53] M. C. Geisler, J. H. Smet, V. Umansky, K. von Klitzing, B. Naundorf, R. Ketzmerick, and H. Schweizer. Detection of a landau band-coupling-induced rearrangement of the hofstadter butterfly. *Phys. Rev. Lett.*, 92:256801, Jun 2004.
- [54] B. Hunt, J. D. Sanchez-Yamagishi, A. F. Young, M. Yankowitz, B. J. LeRoy, K. Watanabe, T. Taniguchi, P. Moon, M. Koshino, P. Jarillo-Herrero, and R. C. Ashoori. Massive Dirac Fermions and Hofstadter Butterfly in a van der Waals Heterostructure. *Science*, 340:1427, 2013.
- [55] P. Zoller D. Jaksch. Creation of effective magnetic fields in optical lattices: the hofstadter butterfly for cold neutral atoms. *New Journal of Physics*, 5(1):56, 2003.
- [56] M. Aidelsburger, M. Atala, M. Lohse, J. T. Barreiro, B. Paredes, and I. Bloch. Realization of the hofstadter hamiltonian with ultracold atoms in optical lattices. *Phys. Rev. Lett.*, 111(18):185301–, October 2013.
- [57] Hirokazu Miyake, Georgios A. Siviloglou, Colin J. Kennedy, William Cody Burton, and Wolfgang Ketterle. Realizing the harper hamiltonian with laser-assisted tunneling in optical lattices. *Phys. Rev. Lett.*, 111:185302, Oct 2013.

- [58] Gregor Jotzu, Michael Messer, Remi Desbuquois, Martin Lebrat, Thomas Uehlinger, Daniel Greif, and Tilman Esslinger. Experimental realization of the topological haldane model with ultracold fermions. *Nature*, 515(7526):237–240, Nov 2014.
- [59] M Aidelsburger, M Lohse, C Schweizer, M Atala, J T Barreiro, S Nascimbène, N. R. Cooper, I. Bloch, and N. Goldman. Measuring the Chern number of Hofstadter bands with ultracold bosonic atoms. *Nature Physics*, 11(2):162–166, December 2014.
- [60] M. Mancini, G. Pagano, G. Cappellini, L. Livi, M. Rider, J. Catani, C. Sias, P. Zoller, M. Inguscio, M. Dalmonte, and L. Fallani. Observation of chiral edge states with neutral fermions in synthetic hall ribbons. *Science*, 349(6255):1510–, Sep 2015.
- [61] M Hafezi, S Mittal, J Fan, A Migdall, and J M Taylor. Imaging topological edge states in silicon photonics. *Nat. Photon.*, 7(12):1001–1005, October 2013.
- [62] A. Celi, P. Massignan, J. Ruseckas, N. Goldman, I.B. Spielman, G. Juzeliunas, and M. Lewenstein. Synthetic gauge fields in synthetic dimensions. *Phys. Rev. Lett.*, 112(4):043001–, Jan 2014.
- [63] B. K. Stuhl, H.-I. Lu, L. M. Aycock, D. Genkina, and I. B. Spielman. Visualizing edge states with an atomic bose gas in the quantum hall regime. *Science*, 349(6255):1514–, Sep 2015.
- [64] Y. Aharonov and D. Bohm. Significance of electromagnetic potentials in quantum theory. *Phys. Rev.*, 115:485, 1959.
- [65] Yakir Aharonov and Ady Stern. Origin of the geometric forces accompanying berry’s geometric potentials. *Phys. Rev. Lett.*, 69(25):3593–3597, 1992.

- [66] Dario Hügel and Belén Paredes. Chiral ladders and the edges of quantum Hall insulators. *Phys. Rev. A*, 89(2):023619, 2014.
- [67] P G Harper. Single band motion of conduction electrons in a uniform magnetic field. *Proceedings of the Physical Society. Section A*, 68(10):874, 1955.
- [68] Gretchen K. Campbell, Jongchul Mun, Micah Boyd, Erik W. Streed, Wolfgang Ketterle, and David E. Pritchard. Parametric amplification of scattered atom pairs. *Phys. Rev. Lett.*, 96:020406, Jan 2006.
- [69] Samuel Mugel, Alexandre Dauphin, Pietro Massignan, Leticia Tarruell, Maciej Lewenstein, Carlos Lobo, and Alessio Celi. Measuring chern numbers in hofstadter strips. *SciPost*, 2017.
- [70] Zhoushen Huang and Daniel P. Arovas. Entanglement spectrum and wannier center flow of the hofstadter problem. *Phys. Rev. B*, 86:245109, Dec 2012.
- [71] Xiong-Jun Liu, K. T. Law, T. K. Ng, and Patrick A. Lee. Detecting topological phases in cold atoms. *Phys. Rev. Lett.*, 111:120402, Sep 2013.
- [72] Lei Wang, Alexey A. Soluyanov, and Matthias Troyer. Proposal for direct measurement of topological invariants in optical lattices. *Phys. Rev. Lett.*, 110(16):166802–, Apr 2013.
- [73] Dan-Wei Zhang and Shuai Cao. Measuring the spin chern number in time-reversal-invariant hofstadter optical lattices. *Physics Letters A*, 380(42):3541–3545, Oct 2016.
- [74] Mahito Kohmoto. Zero modes and the quantized hall conductance of the two-dimensional lattice in a magnetic field. *Phys. Rev. B*, 39:11943–11949, Jun 1989.

- [75] M. Eric Tai, Alexander Lukin, Matthew Rispoli, Robert Schittko, Tim Menke, Dan Borgnia, Philipp M. Preiss, Fabian Grusdt, Adam M. Kaufman, and Markus Greiner. Microscopy of the interacting harperhofstadter model in the two-body limit. *Nature*, 546:519–, June 2017.
- [76] S. Greschner, M. Piraud, F. Heidrich-Meisner, I. P. McCulloch, U. Schollwöck, and T. Vekua. Spontaneous increase of magnetic flux and chiral-current reversal in bosonic ladders: Swimming against the tide. *Phys. Rev. Lett.*, 115:190402, Nov 2015.
- [77] S. Greschner, M. Piraud, F. Heidrich-Meisner, I. P. McCulloch, U. Schollwöck, and T. Vekua. Symmetry-broken states in a system of interacting bosons on a two-leg ladder with a uniform abelian gauge field. *Phys. Rev. A*, 94:063628, Dec 2016.
- [78] Marcello Calvanese Strinati, Eyal Cornfeld, Davide Rossini, Simone Barbarino, Marcello Dalmonte, Rosario Fazio, Eran Sela, and Leonardo Mazza. Laughlin-like states in bosonic and fermionic atomic synthetic ladders. *Phys. Rev. X*, 7:021033, Jun 2017.
- [79] Siddharth A. Parameswaran, Rahul Roy, and Shivaji L. Sondhi. Fractional quantum hall physics in topological flat bands. *Comptes Rendus Physique*, 14(9):816–839, 2013.